Annu. Rev. Nucl. Part. Sci. 1999. 49:633–85

INCLUSIVE JET AND DIJET PRODUCTION AT THE TEVATRON

Gerald C. Blazey
Department of Physics, Northern Illinois University, DeKalb, Illinois 60119;
e-mail: gblazey@niu.edu

Brenna L. Flaugher
Fermi National Accelerator Laboratory, Batavia, Illinois 60115;
e-mail: brenna@fnal.gov

Key Words cross sections, mass and angular distributions, compositeness, QCD, scaling, parton distribution functions

■ **Abstract** High-energy jet distributions measured since 1992 at the Fermilab Tevatron proton-antiproton collider are presented and compared with theoretical predictions. The statistical uncertainties on these measurements are significantly reduced relative to previous results. The systematic uncertainties are comparable in size to the uncertainty in the theoretical predictions. Although some discrepancies between theory and measurements are noted, the inclusive jet and dijet cross sections can be described by quantum chromodynamics. Prospects for reducing the uncertainty in the theoretical predictions by incorporating Tevatron measurements into the proton parton distributions are discussed. Dijet distributions, in excellent agreement with quantum chromodynamics, set a 2.5-TeV limit on the mass scale of quark constituents.

CONTENTS

0163-8998/99/1201-0633$08.00

1. INTRODUCTION

In the past seven years, quantum chromodynamics (QCD), the accepted theory of quark and gluon interactions, has been confronted with a set of precise and varied measurements of jet production from the Tevatron $p\bar{p}$ collider at Fermi National Accelerator Laboratory. In $p\bar{p}$ collisions, jet production can be understood as a point-like collision of a quark or gluon from the proton and a quark or gluon from the antiproton. After the collision, these scattered partons fragment into jets of particles. The extremely high energy of these interactions provides an excellent opportunity to test our understanding of perturbative QCD (pQCD). In particular, differences between QCD calculations and measured jet processes reveal information about both the parton content of the proton and the nature of the strong interaction. Further, unexpected deviations may signal the existence of new particles or interactions down to distance scales of 10^{-19} m or less.

Historically, jet measurements have involved tests of QCD at the highest energies and searches for new physics. Prior to 1992, the inclusive jet cross section, one of the most important hadron collider results, had been measured at the ISR pp collider at a center-of-mass energy of $\sqrt{s} = 63$ GeV (1), at the CERN $p\bar{p}$ collider at 546 and 630 GeV (2, 3), and at the Fermilab Tevatron $p\bar{p}$ collider at 1800 GeV (4, 5). These data span a factor of 20 in beam energy and a factor of 200 in jet energy transverse to the proton beam (E_T) and, in general, are reasonably well described by QCD.

Studies of the correlations between the leading two jets of an interaction also test QCD and provide opportunities to search for new physics. Measurements of dijet distributions prior to 1992, such as the invariant mass of the leading two jets or the angular separation between the jets, are also in good agreement with QCD (6–10). Applying the model of Eichten et al (11), these data are used to search for composite quarks (2–5, 8–10), with the best limits coming from an inclusive jet cross-section

measurement (5). In this model, excess jet production at large E_T relative to QCD is interpreted as the product of quark constituent scattering. Because these data sets are relatively small, all searches are limited by statistical precision rather than by systematic uncertainties at the highest E_T. The review of QCD by Huth & Mangano (12) provides a summary of these inclusive jet and dijet results.

In 1992, with the advent of high-luminosity data collection at the Tevatron, an era of precision $p\bar{p}$ jet physics began. In 1992–1993 (Run 1A), each of the two collider experiments recorded $\approx$20 pb^{-1} of data, and in 1994–1996 (Run 1B) each accumulated $\approx$100 pb^{-1}. Both data sets were recorded at $\sqrt{s} = 1800$ GeV. At the end of Run 1B, a small portion of data ($\approx$600 nb^{-1}) was taken at $\sqrt{s} = 630$ GeV. The two runs together represent a data set $\approx$50 times larger than any preceding data set.

In contrast to previous tests of QCD, the Run 1 jet measurements have statistical uncertainties significantly smaller than experimental or theoretical systematic uncertainties. In fact, the inclusive jet analysis from the Run 1A sample yielded a significant discrepancy between data and contemporaneous theoretical predictions, as well as good agreement with previous measurements (13). In addition to stimulating great excitement over the possibility of departures from QCD, the result motivated a reevaluation of the uncertainties associated with inclusive jet cross-section calculations (14–16). Later measurements of the inclusive jet cross section using the Run 1B samples stimulated further discussions, since one confirmed (e.g. 17) the earlier measurement whereas the other was well described by QCD. In addition, subsequent studies have indicated that QCD can describe the observed Run 1A cross section through adjustments to the parton distribution functions (PDFs), which describe the fraction of proton momentum carried by the constituent quarks and gluons.

Independent of the actual high-E_T behavior of the inclusive jet cross section, the Run 1A and 1B results revealed large uncertainties in the theoretical predictions. In particular, the PDFs were derived from fits to data from many different experiments, all of which are collected at low energy and extrapolated to Tevatron jet energies. Representation of the uncertainties in the resulting PDFs is a complex issue and has never been precisely resolved. Consequently, the Tevatron collaborations have taken an interest the PDFs derived from information collected at the Tevatron. Measurements of dijet mass distributions and dijet cross sections at a variety of scattering angles provide information on the momentum distributions of the partons. Comparison of the different measurements can establish constraints on the PDFs, ultimately improving sensitivity to the presence of new physics.

This review opens with a description of the theoretical framework behind pQCD and a discussion of the uncertainties associated with predictions. The chapter also describes the two detectors in which these measurements were performed and explains jet reconstruction algorithms. We devote sections to the Run 1 measurements of the inclusive jet cross section, the ratio of inclusive cross sections at different beam energies, dijet differential cross sections, and dijet mass and angular distributions. These measurements offer a detailed look into the composition of

the proton and the nature of the strong interaction. Our conclusion summarizes the results and suggests future avenues of research.

2. PERTURBATIVE QUANTUM CHROMODYNAMICS

2.1 Leading-Order and Next-to-Leading-Order Quantum Chromodynamics

The $p\bar{p}$ interaction, a fairly general scattering process, makes a good introduction to the concepts of leading-order and next-to-leading-order pQCD. As illustrated in Figure 1, inelastic scattering between a proton and an antiproton can be described as an elastic collision between a single constituent of the proton and a single constituent of the antiproton. These constituents are collectively referred to as partons and in QCD are quarks and gluons. The noncolliding constituents of the incoming proton and antiproton are called beam fragments or spectators. Predictions for jet production are given by folding experimentally determined PDFs f with perturbatively calculated two-body scattering cross sections $\hat{\sigma}$ (see e.g. 19 for a detailed discussion). The two ingredients can be formally combined to calculate any cross section of interest:

$$\sigma = \sum_{i,j} \int dx_1 dx_2 \, f_i(x_1, \mu_F^2) \, f_j(x_2, \mu_F^2) \hat{\sigma}\left[x_1 P, x_2 P, \alpha_s(\mu_R^2), Q^2/\mu_F^2, Q^2/\mu_R^2\right].$$

The PDFs $f_k(x, \mu_F^2)$ describe the momentum fraction x of the incident hadron momentum P carried by a parton of type k (gluons or quarks). The PDF is defined in terms of the factorization scale μ_F. The hard two-body cross section is a function of the momentum carried by each of the incident partons xP, the strong coupling parameter α_s, the scale Q^2 characterizing the energy of the hard interaction, and the renormalization scale μ_R. Final-state partons manifest themselves as collimated streams (jets) of particles. This formal description includes no explicit

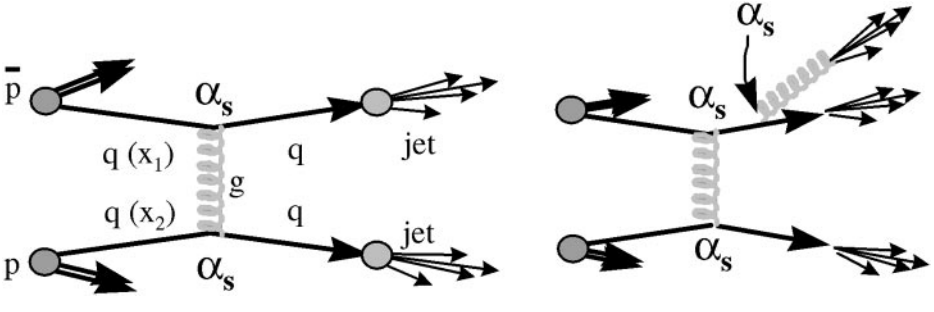

Figure 1 Factorization of the scattering process. In this example, incoming quarks with momentum fraction x_1 and x_2 of the incident hadrons scatter through gluon exchange and fragment into final-state jets.

hadronization or fragmentation functions to describe the transition from partons to jets. For most high-E_T measurements, these effects are small and jets are identified as partons.

Figure 1 illustrates the two-body scattering with a leading-order (LO) graph. The cross section for this process is proportional to two powers of the strong coupling parameter, α_s, which come from the two vertices. Although useful, the LO picture is too simple and has large normalization uncertainties. Next-to-leading-order (NLO) or $O(\alpha_s^3)$ calculations include one additional parton emission. The second diagram in Figure 1 gives an example. Here a final-state quark has radiated an additional gluon, and the entire scattering process is proportional to α_s^3. Depending on the proximity of the other partons, a jet can be formed from one or two (combined) partons. This additional radiation in turn results in parton-level predictions for the shape of jets, and for the effects of clustering parameters.

A complete theoretical prediction of jet production should not depend on internal calculational details; however, this is not the case for fixed-order pQCD, which depends on the choice of factorization and renormalization scales. The factorization scale, a free parameter, determines how the contributions of initial-state radiation are factorized between the PDFs and $\hat{\sigma}$. The renormalization scale is also arbitrary and is related to choices in the theoretical calculations designed to control or renormalize ultraviolet singularities. Typically, as in this report, μ_R and μ_F are set equal to each other, $\mu_R = \mu_F = \mu$, and μ is chosen to be of the same order as Q. The sensitivity of the theoretical predictions to μ is often taken as a measure of the uncertainty from the contributions of higher-order terms.

Ellis et al (20), Aversa et al (21), and Giele et al (22) have derived predictions for jet production at NLO. The NLO predictions are much less sensitive to the choice of μ (20). The EKS program by Ellis et al (23) can generate analytic predictions for jet cross sections as a function of final-state parameters. The JETRAD program by Giele et al (24) generates weighted events with final-state partons. Cross sections are calculated by generating a large number of events as a function of final-state parameters. All predictions in this chapter have been generated either with EKS or JETRAD. The two programs agree to within a few percent (16).

2.2 Theoretical Choices

A NLO QCD calculation requires selection of several input parameters, including specification of a parton clustering algorithm, a perturbative scale, and PDFs. Taken together, these choices can result in approximately 30% variations in the theoretical predictions. The single largest uncertainty arises from the PDFs. The variations are illustrated by comparing predictions for the inclusive jet cross section. As in the experimental results, the cross section is reported as a function of jet transverse energy (E_T) and pseudorapidity $\eta = -\ln(\tan(\theta/2))$, where θ is the angle between the jet and the proton beam and is summed over ϕ, the azimuthal angle around the beam. For reference, $\eta = 0$ for jet production at 90 degrees relative to the proton beam.

2.2.1 Parton Clustering The NLO predictions may include two or three final-state partons. To convert the partons to the jets measured in a detector, a clustering algorithm is used. The Snowmass cone algorithm (25) was proposed to minimize the difference between theoretical predictions and experimental measurements. In theoretical calculations, two partons that fall within a cone of radius R in η–ϕ space ($R = \sqrt{\Delta\eta^2 + \Delta\phi^2}$ and $\Delta\eta$ and $\Delta\phi$ are the separation of the partons in pseudorapidity and azimuthal angle) are combined into a jet. Both collider experiments use a standard cone radius of $R = 0.7$ for most measurements. A consequence of this algorithm is that partons have to be at least $2R$ apart to be treated as separate jets.

Subsequent studies indicated that the experimental clustering algorithms (described in later sections) were more efficient at separating nearby jets (26, 27) than was the idealized Snowmass algorithm. In other words, the experimental clustering algorithms could identify two jets separated by less than $2R$. An additional parameter, $R_{\rm sep}$, was introduced in the QCD predictions to mimic the experimental effects of cluster merging and separation. Partons within $R_{\rm sep} \times R$ were merged into a jet, whereas partons separated by more than $R_{\rm sep} \times R$ were identified as two individual jets. A value of $R_{\rm sep} = 1.3$ was found to give the best agreement with the data for cross-section and jet shape measurements (26). This corresponds in the data to 50% efficiency in jet separation (27); that is, two jets within $1.3R$ of one another are merged 50% of the time and are identified as two individual jets 50% of the time. At separations of $1.0R$ the algorithms nearly always merge the two jets, and at $1.6R$ they nearly always identify two separate jets. Figure 2 (*top*) shows the change in the prediction, using the EKS program, for the inclusive jet cross section when $R_{\rm sep}$ is decreased from 2 to 1.3. The result is primarily a normalization change of 5–7%.

2.2.2 The Scale Because a NLO calculation is truncated at order α_s^3, there is some residual dependence on the scale μ at which the calculation is performed. The scale is usually taken to be proportional to $E_T^{\rm jet}$ (or just E_T), the maximum transverse jet energy $E_T^{\rm max}$ in a given event, or the total center-of-mass energy. Other choices for the scale are possible. To study the scale dependence of the predictions, the magnitude of the scale is varied by a multiplicative coefficient; common choices are $\mu = 0.5E_T^{\rm jet}$ and $0.5E_T^{\rm max}$. Figure 2 (*middle*) shows a mild E_T dependence at the 2–9% level on the definition of the scale. The figure (*bottom*) also shows that typical variations of the multiplicative coefficient lead to 5–20% shifts in the cross section with only small changes in shape above 100 GeV.

2.2.3 Parton Distribution Functions PDFs are derived from global fits to data primarily from deep inelastic scattering (DIS) fixed target and electron-proton collider experiments. In DIS, a lepton probe is used to sample the partonic structure of the target hadrons. For use at the Tevatron, the resulting distributions must be evolved from the low-energy DIS results to the high-energy range of jet measurements.

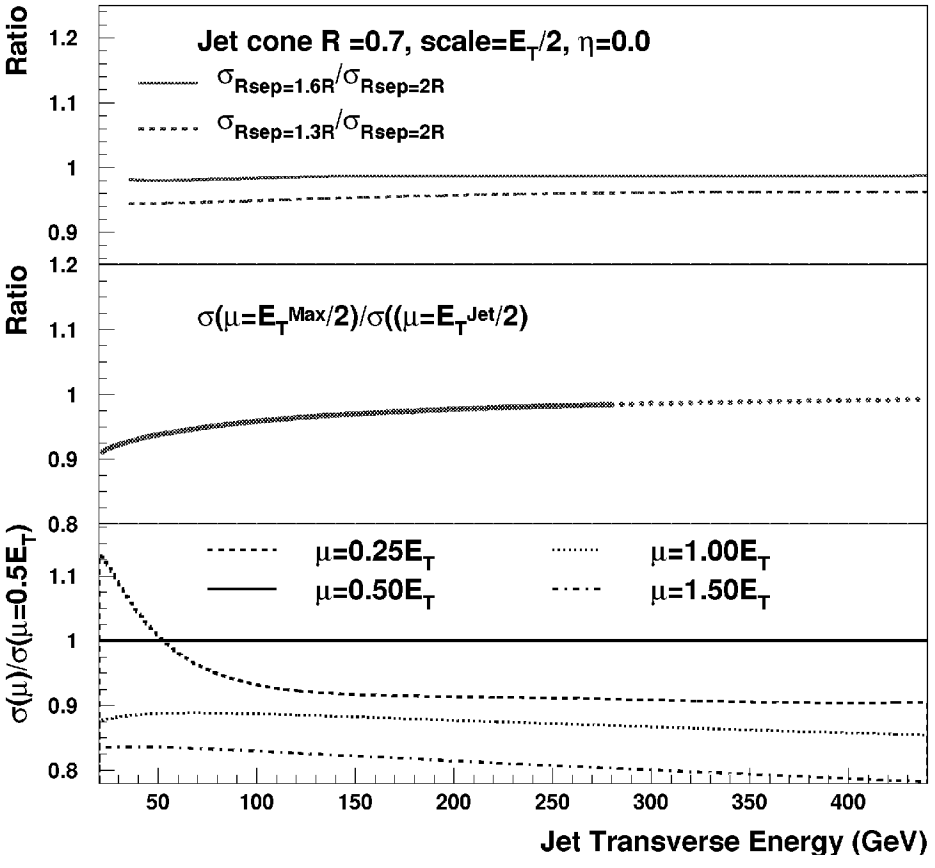

Figure 2 Next-to-leading-order (NLO) theoretical predictions for the inclusive jet cross section. Each prediction is normalized relative to the NLO EKS calculation with CTEQ4M, $\mu = E_T^{\text{jet}}/2$, $R_{\text{sep}} = 1.3$.

As the data from DIS experiments increase and improve, new parton distribution functions are derived. Some recent PDF derivations also incorporate data from the Tevatron. The result is a plethora of PDFs, each with its own specific list of data included in the fit, assumptions as to the value of α_s, functional forms for the quark and gluon momentum distributions, and assumptions concerning the contributions of the gluons, which are not constrained by the DIS results. The most recent PDFs include the most precise data and combined knowledge, supplanting the previous PDFs.

Several groups have analyzed the available data and produced families of candidate PDFs. Within a family, the individual PDFs represent the range of predictions resulting from changes in one of the input assumptions, such as the value of α_s. Additional variations come from differences in the input data sets or the relative

weighting between the data sets. The CTEQ2M (28), CTEQ3M (29), and MRSA′ (30) families of PDFs incorporate data published before 1994 and do not include Tevatron jet data. The CTEQ4M PDFs (31) include data published before 1996; CTEQ4HJ (31) additionally has a high-x gluon adjustment designed to accommodate the Run 1A high-E_T jet cross-section measurements. The MRST (32) PDF family uses data published before 1998 and adds a contribution for a putative initial transverse momentum of the partons.

Comparison between observed cross sections and NLO predictions with alternate PDFs provide some insight into the quark and gluon composition of the proton. As Figure 3 shows, the PDFs can result in ≈20% variations in jet cross

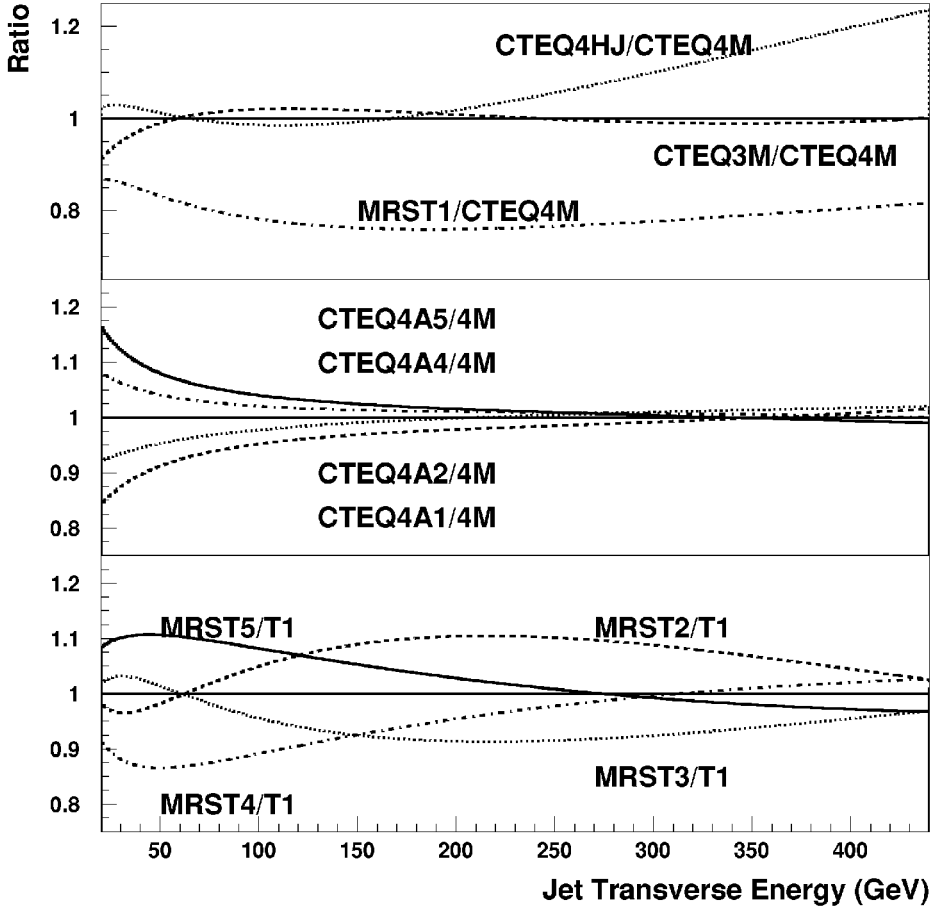

Figure 3 Next-to-leading-order (NLO) theoretical predictions for the inclusive jet cross section using different parton distribution functions. Each prediction is normalized relative to the NLO EKS calculation with CTEQ4M. They all use $\mu = E_T/2$ and $R_{\text{sep}} = 1.3$.

sections; typical variations within a set are on the order of 5–10%. Although the quark distributions were thought to be well known and the contribution of the gluons was expected to be small, investigations (33, 34) have shown that there are uncertainties at high x, which were ignored in the derivation of early PDFs. In addition, studies (31) revealed that the gluon distribution could be adjusted to give a significant increase in the jet cross section at high E_T while maintaining reasonable agreement with the low-energy data.

3. DETECTORS AND JET DEFINITIONS

3.1 The CDF and DØ Detectors

The Collider Detector at Fermilab (CDF) (35) and the DØ Detector (36) are complementary general-purpose detectors designed to study a broad range of particle physics topics. The Tevatron has six locations at which the counter-rotating proton and antiproton beams can collide. The CDF and DØ detectors each occupy one of these interaction regions (DØ takes its name from the alphanumeric designation of its interaction region). Each detector is composed of a series of concentric subsystems that surround the $p\bar{p}$ interaction region. Immediately outside the Tevatron beam pipe, each detector has a tracking system to detect charged particles. The tracking systems are surrounded by calorimeters, which measure the energy and direction of electrons, photons, and jets. The calorimeters are surrounded by muon-tracking systems.

Luminosity monitors at each detector measure the beam exposure. These monitors are located near the beamlines and detect particles from the $p\bar{p}$ collisions. The luminosity at a given site is derived from the ratio of the measured event rate to the total $p\bar{p}$ cross section integrated over the counter acceptance. A direct comparison of jet cross sections at the two experiments is complicated by the fact that the collaborations adopted slightly different values for the total $p\bar{p}$ cross section (37–39). As a result, the CDF jet cross-section measurements are 2.7% higher than the corresponding DØ jet cross-section measurements (37).

The following sections focus primarily on the central tracking systems and the calorimeters because these systems are the most important for jet identification and reconstruction. CDF has a high-resolution particle tracking system, which makes a crucial contribution to jet energy calibration. On the other hand, and in a complementary fashion, DØ has highly segmented, uniform, and thick calorimetry well suited to in-situ jet energy measurements.

Both calorimeters are segmented into projective towers. Each tower points back to the center of the nominal interaction region and is identified by its pseudorapidity and azimuth. The polar angle θ in spherical coordinates is measured from the proton beam axis, and the azimuthal angle ϕ is measured from the plane of the Tevatron. The towers are further segmented longitudinally into individual readout cells. The energy of a calorimeter tower is obtained by summing the energy in all the cells of the same pseudorapidity and azimuth. The E_T of a tower is the sum of the E_T

components of the cells. These components are calculated by assigning each cell of a tower a massless four-vector with magnitude equal to the energy deposited and with the direction defined by the unit vector pointing from the event origin to the center of the tower segment.

3.1.1 DØ in Run 1 The central tracking volume ($|\eta| \approx 2$) of DØ includes the vertex chamber, transition radiation detector, and central drift chamber, arranged in three cylinders concentric with the beamline, as well as two forward drift chambers. The nonmagnetic tracker is compact, with an outer radius of 75 cm and an overall length of 270 cm centered on $z = 0$. Without the need to measure momenta of charged particles, the prime considerations for tracking are good two-track resolving power, high efficiency, and good ionization energy measurement. For jet physics, the central tracker is used to find event vertices.

Jet detection in the DØ detector primarily uses liquid argon-uranium calorimeters, which are hermetic, finely segmented, thick, and uniform, and which have unit gain. These sampling calorimeters are composed of alternating layers of liquid argon and absorber. The particles in a jet interact with the absorber, and the resulting particle shower ionizes the liquid argon. This ionization is detected as a measure of the jet energy. The calorimeter is enclosed in three cryostats: the central calorimeter (CC) covers $|\eta| \leq 1.2$, and the end calorimeters (ECs) extend the coverage to $|\eta| \leq 4.4$. The calorimeters have complete 2π azimuthal coverage. Between the cryostats, the calorimeter sampling is augmented by scintillator tiles with segmentation matching the argon calorimeters. Figure 4 is a graphic representation of the calorimeter modules described below.

The CC includes three concentric rings of calorimeter modules. There are 32 electromagnetic calorimeter modules (CCEM) in the inner ring, 16 fine hadronic modules (CCFH) in the middle ring, and 16 coarse hadronic modules (CCCH) in the outer ring. The CCEM and CCFH calorimeters have uranium absorber plates, and the CCCH has copper absorber plates. Longitudinal segmentation includes eight samples: four in the CCEM, three in the CCFH, and one in the CCCH. At $\eta = 0$, the CC has a thickness of 7.2 nuclear absorption lengths. The calorimeter cells are segmented into $\Delta\eta \times \Delta\phi = 0.1 \times 0.1$, except at shower maximum in the third layer of the CCEM, where the segmentation is 0.05×0.05. The calorimeter segmentation is designed to form projective towers of size $\Delta\eta \times \Delta\phi = 0.1 \times 0.1$ geometry that point to $z = 0$. In the CC, because of the finer resolution in the third layer of the CCEM, each tower comprises 11 cells.

The two mirror-image ECs contain four module types. An electromagnetic module (ECEM) surrounding the beam pipe is backed by an inner hadronic module (ECIH), which also surrounds the pipe. Outside the ECEM and ECIH are concentric rings of 16 middle and outer hadronic modules (ECMH and ECOH). The ECEM and ECIH have uranium absorber plates and four longitudinal segments. The ECMH has four uranium absorber segments nearest the interaction point and one stainless steel absorber segment behind. The ECOH uses stainless steel plates

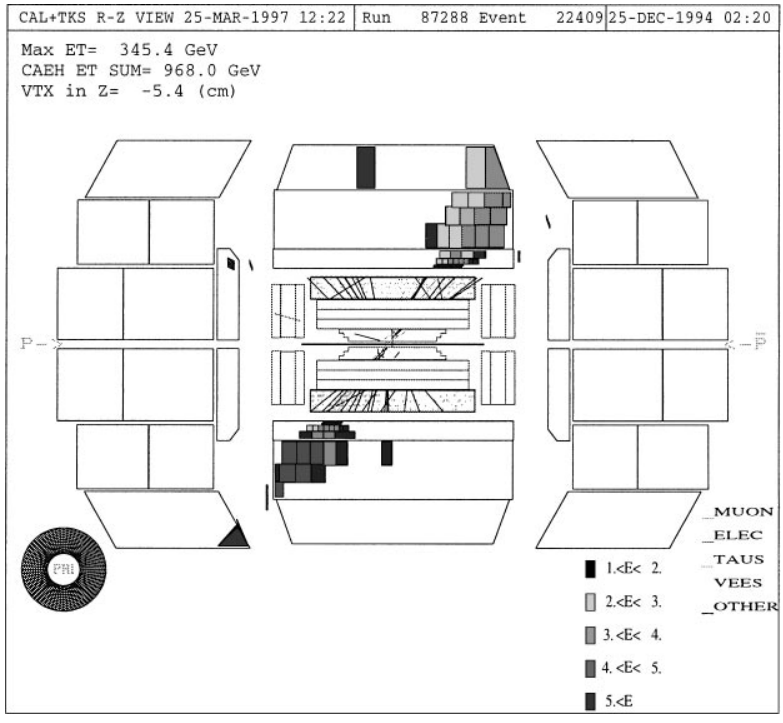

Figure 4 The distribution of energy in a dijet event in the DØ detector.

and includes three longitudinal segments. At $|\eta| = 2.0$, a jet encounters 8–9 longitudinal segments and a nuclear interaction thickness of $\approx 10\lambda_o$. The transverse segmentation is similar to that of the CC. The CC(EC) energy resolution for electrons is 14.8 (15.7)%/$\sqrt{E}$ plus 0.3(0.3)% added in quadrature and for hadrons 47.0(44.6)%/$\sqrt{E}$ plus 4.5 (3.9)% added in quadrature.

The calorimeter response to the different types of particles is the most important aspect of the DØ jet energy calibration. Electromagnetically interacting particles such as photons (γ) and electrons deposit most of their energy in the electromagnetic sections of the calorimeters. Hadrons, by contrast, lose energy primarily through nuclear interactions and extend over the full interaction length of the calorimeter. In general, the calorimeter response to the electromagnetic (e) and nuclear or hadronic components (h) of hadron showers is not the same. Noncompensating calorimeters have a response ratio e/h greater than one and suffer from non-Gaussian event-to-event fluctuations in the fraction of energy lost through electromagnetic production. Such calorimeters give a non-Gaussian signal distribution for hadrons and jets. The DØ calorimeter is nearly compensating and the hadronic and jet response are well described by a Gaussian distribution (40). In fact, single-jet resolution as measured with dijet events has a Gaussian line-shape

and is approximately 7% at 100 GeV and 5% at 300 GeV (M Bhattacharjee, unpublished thesis).

The DØ jet calibration requires correction for the hadronic response of the jet, showering of energy outside the cone, and subtraction of an offset (which can be attributed to instrumental effects, pile-up from previous beam-beam crossings, additional interactions, and spectator energy). These corrections are derived primarily in situ (40). The correction for hadronic response begins with the electromagnetic calibration of the calorimeter, which is performed with dielectron and diphoton decays of the Z and π^0 resonances, since electrons and photons deposit their energy in the electromagnetic calorimeters. The hadronic response for centrally produced γ-jet events is derived from data using E_T balance between the photon and jet. At $\eta = 0$, the hadronic response for a 100-GeV jet of cone size 0.7 is $0.85 \pm 0.01\%$. The response is below unity because of the intermodule cracks. The rapidly falling γ–jet cross section limits the balance technique in the central calorimeter to jet energies below 150 GeV. Balancing central, well-measured photons against high-rapidity jets extends the energy calibration to 300 GeV. Above 300 GeV, the response calibration uses simulated γ–jet events. The showering correction for a 100-GeV jet at $\eta = 0$ is about $1 \pm 1\%$ and is derived from a study of jet profiles. The total offset correction, as determined from a study of data sets with various triggering and luminosity conditions, is about 2.6 ± 0.3 GeV, including the contribution from the underlying event or spectator energy of roughly 0.9 ± 0.1 GeV. At $\eta = 0$ the mean total energy correction for a $R = 0.7$, 100-GeV jet is $15.0 \pm 1.7\%$ and decreases slowly with energy.

3.1.2 CDF in Run 1 The CDF central ($|\eta| \approx 1$) tracking system has three subsystems located within a 1.4-T magnetic field, which is provided by a superconducting solenoid coaxial with the beam. Nearest the beam, a four-layer silicon microstrip vertex (SVX) detector (42) occupies the radial region between 3.0 cm and 7.9 cm from the beamline and provides precision $r - \phi$ measurements. Outside the SVX, a vertex drift chamber (VTX) provides $r - z$ tracking information and is used to locate the position of the $p\bar{p}$ interaction (event vertex) in z along the beamline. Both the SVX and the VTX are mounted inside a 3.2-m-long drift chamber called the central tracking chamber (CTC). The radial coverage of the CTC is from 31 cm to 132 cm. The momentum resolution (35) of the SVX–CTC system is $\delta P_T / P_T^2 = [(0.0009 P_T)^2 + (0.0066)^2]^{1/2}$, where P_T is measured in units of GeV/c. The CTC provides in-situ measurement of the calibration and response of the calorimeter to low-energy particles (where test beam information is not available), along with measurements of jet fragmentation properties.

The solenoid and tracking volumes of CDF are surrounded by calorimeters, which cover 2π in azimuth and $|\eta| \leq 4.2$. The central electromagnetic (CEM) calorimeter covers $|\eta| \leq 1.1$ and is followed at a larger radius by the central hadronic calorimeters (CHA and WHA), which cover $|\eta| \leq 1.3$. These calorimeters use scintillator as the active medium. The CEM absorber is lead and the CHA/WHA absorber is iron. The calorimeters are segmented into units of 15

degrees in azimuth and 0.1 pseudorapidity. Two phototubes bracket each tower in ϕ, and the average of the energy in the two tubes is used to determine the ϕ position of energy deposited in a tower. The interaction length of both the CHA and WHA is $4.5\lambda_o$. Electron energy resolution in the CEM is $13.7\%/\sqrt{E}$ plus 2% added in quadrature. For hadrons, the single-particle resolution depends on angle and varies from roughly $50\%/\sqrt{E}$ plus 3% added in quadrature in the CHA to $75\%/\sqrt{E}$ plus 4% added in quadrature in the WHA. In the forward regions ($1.1 < |\eta| < 4.2$), calorimetric coverage is provided by gas proportional chambers. The plug electromagnetic (PEM) and hadronic calorimeters (PHA) cover the region $1.1 < |\eta| < 2.4$. The forward electromagnetic (FEM) and hadronic calorimeters (FHA) cover the region $2.2 < |\eta| < 4.2$. The segmentation of these detectors is roughly 0.1 in η and 5 degrees in ϕ.

Figure 5 shows a three-jet event in the CDF calorimeter. In this "lego" plot, the calorimeter is "rolled out" onto the η–ϕ plane. The tower height is proportional to the E_T deposited in the tower.

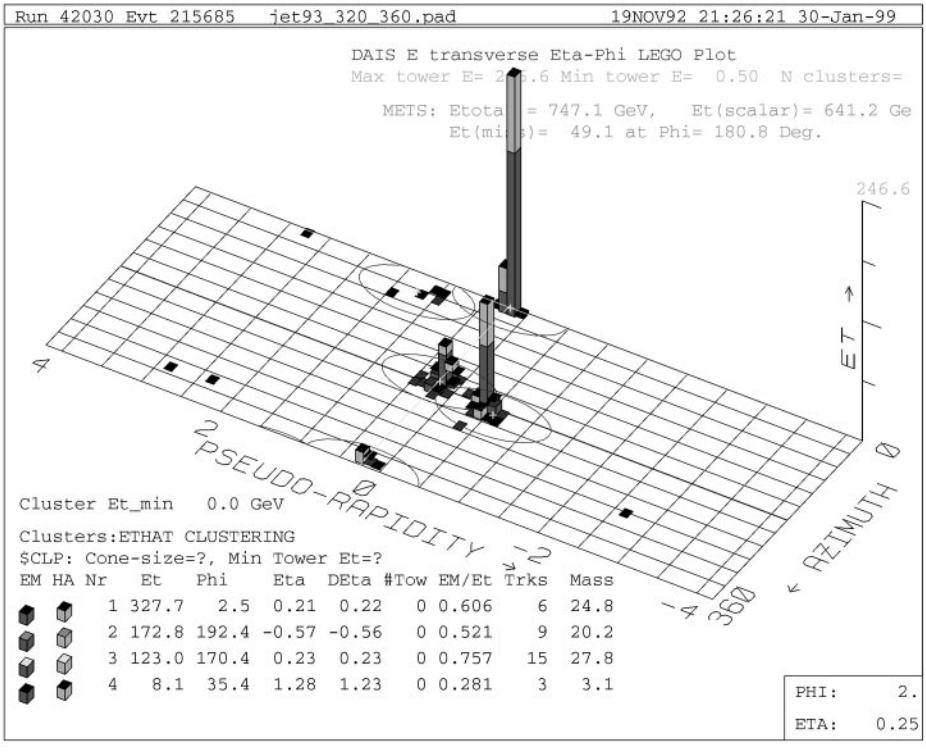

Figure 5 A three-jet event in the CDF detector. Dark shading, E_T of electromagnetic cells of the tower; light shading, E_T of hadronic cells of the tower. The oval around each clump of energy indicates the jet-clustering cone of $R = 0.7$.

Observed jet energies are corrected for a number of effects, including the calibration and response of the detectors and the background energy from the remnants of the $p\bar{p}$ interaction. In the central detectors, corrections associated with detector response are obtained from a Monte Carlo simulation, which is tuned to give good agreement with the data from electron and hadron test beams (E_{beam} varies from 10 GeV to 227 GeV), and to data from an in-situ study using CTC track momenta and isolated hadrons with 400 MeV/c $< P_T <$ 10 GeV/c. In addition, the Monte Carlo jet fragmentation parameters are tuned to agree with both the number and momenta of particles observed in jets. The resulting simulation is then used to determine response functions, which represent the response of the calorimeter to jets as a function of jet E_T. The width of the response functions represents the jet energy resolution and can be expressed as $\sigma = 0.1E_T + 1$ GeV (5). Calibration of the plug and forward detectors is achieved through a dijet energy balancing technique (43). The E_T of jets in the plug and forward detectors is balanced against jets in the central region whose calibration is pinned by the tracking information. The energy left in a jet cone from the hard interaction spectators is called the underlying event energy. No precise theoretical definition of this quantity exists. Experimentally, it has been estimated from events in which there is no hard scattering and from the energy in cones perpendicular to the jet axis in dijet events. For a cone of radius 0.7, the contribution to the jet E_T is of the order of 1 GeV. An uncertainty of 30% is assigned to this quantity to cover reasonable variations in its definition. The magnitude of the total jet energy corrections and the corresponding uncertainty depend on the E_T of the jets and their location in the detector, as well as on the specific analysis. Typically, the jet E_T correction factor is in the range of 1.0 to 1.2.

3.1.3 CDF and DØ in Run 2 The Fermilab Tevatron is undergoing major improvements for Run 2, which is slated to begin in the year 2000. The energy of the proton and antiproton beams will increase from 900 to 1000 GeV and the instantaneous luminosity will increase by at least a factor of five. The expected Run 2 data sample is $2\,fb^{-1}$ in the first two years of operation.

Both the CDF and DØ collaborations are improving their detectors for Run 2 operations. Among other things, CDF is replacing the gas calorimeters with scintillating tiles and is closing gaps between calorimeters. The new plug calorimeter can be calibrated using tracks, as in the central, due to expanded tracking coverage. DØ is also upgrading a number of detector components. The upgrade most important for jet measurements is the replacement of the nonmagnetic tracking system with a magnetic tracker. The tracker (including a high-resolution silicon strip detector, a scintillating fiber tracker, and electron/photon preshower detectors) will enable calibration of the calorimeter with single particles. Thus, in Run 2 the detectors will be more similar than in Run 1—CDF will have more uniform calorimetry and DØ will have magnetic tracking. The result of these improvements should be an overall reduction of jet measurement uncertainties.

3.2 The Experimental and Theoretical Definitions of a Jet

From the experimental point of view, jets are the manifestation of partons as showers of electromagnetic and hadronic matter. Jets are observed as clusters of energy located in adjacent detector towers. Typically, a jet contains tens of neutral and charged pions (and some kaons), each of which showers into multiple cells. A single jet illuminates roughly 20 towers (this corresponds to approximately 40 calorimeter cells in the CDF detector and over 100 detector cells in the DØ detector). Figure 4 illustrates the energy deposition of a two-jet event in the DØ detector. Each rectangular outline represents the energy deposited in calorimeter cells at fixed η and depth. The eye naturally clusters the energy into two jet-like objects. However, jet cross-section measurements require a more quantitative definition of the jet.

For high-E_T measurements, CDF and DØ use cone algorithms to identify jets in the calorimeters. Cone algorithms operate on objects in pseudorapidity and azimuth space, such as particles, partons, calorimeter cells, or calorimeter towers. For simplicity, the following discussions refer to towers. The CDF and DØ algorithms are both based on the Snowmass algorithm (25), which defines a jet as those towers within a cone of radius $\Delta R = \sqrt{\Delta\phi^2 + \Delta\eta^2} = 0.7$. The jet E_T is the sum of the transverse energies of the towers in the cone, and the location of the jet is defined by the E_T weighted η and ϕ centroids:

$$E_T^{\text{jet}} = \sum_i E_T^i$$

$$\eta_{\text{jet}} = \left(\sum_i E_T^i \, \eta_i \right) \Big/ E_T^{\text{jet}}$$

$$\phi_{\text{jet}} = \left(\sum_i E_T^i \, \phi_i \right) \Big/ E_T^{\text{jet}}.$$

The sum over i is over all towers that are within the jet radius R.

In Figure 5, the clustering cone (shown by the oval around each jet) is centered on the cluster centroid. The two overlapping cones in this event indicate that the two nearby clusters have been identified as two separate jets. The Snowmass algorithm does not specify cell thresholds or the handling of such overlapping jet cones. These details must be dealt with according to the needs of individual experiments.

DØ defines jets in two stages (27). In the first or clustering stage, all the energy that belongs to a jet is accumulated, and in the second stage, the η, ϕ, and E_T of the jet are defined. The clustering consists of the following steps:

1. Calorimeter towers with $E_T \geq 1$ GeV are enumerated. Starting with the highest E_T tower, preclusters are formed by adding neighboring towers within a radius of $R = 0.3$.

2. The jet direction is calculated for each precluster using the sums defined for the Snowmass algorithm.
3. All the energy in the towers in a cone of radius $R = 0.7$ around each precluster is accumulated and used to recalculate η and ϕ.
4. Steps 2 and 3 are repeated until the jet direction is stable.

Finally, in the second stage, the jet energy and directions are calculated according to the following equations:

$$E^{\text{jet}} = \sum_i E^i, \quad E_T^{\text{jet}} = \sum_i E_T^i$$

$$\tan\theta_{\text{jet}} = \frac{\sqrt{\left(\sum_i E_x^i\right)^2 + \left(\sum_i E_y^i\right)^2}}{\sum_i E_z^i}.$$

$$\phi_{\text{jet}} = \tan^{-1}\left[\sum_i E_y^i \Big/ \sum_i E_x^i\right]$$

where $E_x^i = E_i \sin(\theta_i)\cos(\phi_i)$, $E_y^i = E_i \sin(\theta_i)\sin(\phi_i)$, and $E_z^i = E_i \cos(\theta_i)$. Studies have shown that for $\eta \leq \sim 1$, the final DØ jet directions are, within experimental errors, equal to the Snowmass directions. Overlapping jets are merged if more than 50% of the smaller jet E_T is contained in the overlap region. If less than 50% of the energy is contained in the overlap region, the jets are considered two jets and the energy in the overlap region is assigned to the nearest jet. After merging or splitting, the jet directions are recalculated.

The CDF cluster algorithm (44) has two stages of jet identification, similar to those of the DØ algorithm. The first stage consists of the following steps:

1. A list of towers with $E_T > 1.0$ GeV is created.
2. Preclusters are formed from an unbroken chain of contiguous seed towers with continuously decreasing tower E_T. If a tower is outside a window of 7×7 towers surrounding the seed, it is used to form a new precluster.
3. The preclusters are grown into clusters by finding the E_T weighted centroid and collecting the energy from all towers with more than 100 MeV within $R = 0.7$ of the centroid.
4. A new centroid is calculated from the set of towers within the cone and a new cone drawn about this position. Steps 3 and 4 are repeated until the set of towers contributing to the jet remains unchanged.
5. Overlapping jets are merged if they share $\geq$75% of the smaller jet's energy. If they share less, the towers in the overlap region are assigned to the nearest jet.

In the second stage, the final jet parameters are computed. The angles and energy are calculated as in the DØ algorithm, but the jet E_T is given by

$$E_T = E \sin\theta_{\text{jet}}.$$

Studies (25) found that the CDF clustering algorithm and the Snowmass algorithm are numerically very similar. One philosophical difference between the CDF and Snowmass algorithms is that the CDF jets have mass ($E_T \neq P_T$).

Both the CDF and DØ algorithms are based on the Snowmass algorithm, but the reality of jets of hadrons measured by a finitely segmented calorimeter necessitates additional steps and cuts. Apart from small definitional details, the most significant difference between the Snowmass algorithm and its experimental implementations is the handling of cluster merging and separation. To simulate these effects in the NLO calculations, the R_{sep} parameter was introduced. Considering the complexity of the hadronic showers, it is remarkable that a NLO calculation, with only two or three partons in the final state and a single additional parameter, can provide a good description of the observed jet shapes and cross sections (26).

4. THE INCLUSIVE JET CROSS SECTION AT 1800 GeV

4.1 Introduction

The inclusive jet cross section represents one of the most basic tests of QCD at a hadron-hadron collider. It reflects the probability of observing a hadronic jet of a given E_T and rapidity in a $p\bar{p}$ collision. The term inclusive indicates that all the jets in an event are included in the cross-section measurement and that the presence of additional nonjet objects (e.g. electrons or muons) is irrelevant. Theoretical calculations are normally expressed in terms of the invariant cross section

$$E d^3\sigma/dp^3,$$

where E and p are the jet energy and momentum. In terms of the experimental variables, the cross section is given by

$$d^2\sigma/dE_T\, d\eta,$$

which is related to the first expression by

$$E d^3\sigma/dp^3 = (1/2\pi E_T) d^2\sigma/dE_T\, d\eta.$$

Massless jets are assumed ($P_T = E_T$); the 2π comes from the integration over the azimuthal angle ϕ. The measured cross section is simply the number of jets N observed in an η and E_T interval normalized by the total luminosity exposure, $\mathcal{L}$:

$$d^2\sigma/dE_T\, d\eta = N/(\Delta E_T \Delta\eta \mathcal{L}).$$

The CDF and DØ inclusive jet analyses place similar requirements on the events and jets selected for calculation of the cross sections. Both collaborations eliminate poorly measured events by requiring the event vertices to be near the center of the detector. Backgrounds (e.g. cosmic rays) are eliminated by rejecting events with large missing E_T. Spurious jets from cosmic-ray or instrumental backgrounds are eliminated by quality cuts based on jet shapes. Corrections are made

to the measured cross sections to account for the event and jet detection inefficiencies, mismeasurement of the jet energies, and energy falling in a jet cone from other sources (e.g. remnants of the $p\bar{p}$ collision, or additional $p\bar{p}$ interactions). No corrections are made for partons showering outside the jet cone because this phenomenon should be accounted for in the NLO theoretical calculations.

We begin our discussion of the inclusive jet cross section with CDF measurements. The Run 1A measurement stimulated interest because of a discrepancy with QCD predictions at high E_T. A subsequent DØ measurement with Run 1B data is well described by theoretical predictions, whereas the preliminary CDF Run 1B result is in good agreement with the 1A measurement. The next sections describe the CDF and DØ measurements in some detail and compare the two sets of results.

4.2 The CDF Cross Section

In 1996, CDF published the inclusive jet cross section measured from the Run 1A data sample (13) for jet E_T from 15 GeV to 440 GeV in the central rapidity range $0.1 \leq |\eta| \leq 0.7$. This analysis followed the same procedures as previous measurements (4, 5) for correcting the cross section and for estimating the systematic uncertainties. (This process is described briefly below; see 4, 5, 13, 45 for details.)

The measured jet E_T spectrum requires corrections for energy mismeasurement and for smearing effects caused by finite E_T resolution. An "unsmearing" procedure (45) accomplishes these corrections. As mentioned above, a Monte Carlo simulation (5) tuned to the CDF data is used to determine detector response functions. A trial true spectrum is smeared using these response functions and is compared with the raw data. The parameters of the trial spectrum are iterated to obtain the best match between the smeared trial spectrum and the raw data. The corresponding unsmeared curve is referred to as the standard curve and is used to correct the measured spectrum. The simultaneous correction for response and resolution produces a result that is independent of the E_T binning used in the measurement but preserves the statistical uncertainty on the measured cross section. For jet E_T between 50 GeV and about 300 GeV, these corrections increase both the E_T and the cross section by ≈10%. At lower and higher E_T, the cross-section corrections are larger because of the steepening of the spectrum.

Figure 6 shows the CDF measurement of the inclusive jet cross section from the 20 pb^{-1} Run 1A data sample compared with a NLO prediction from the EKS program with $\mu = E_T/2$, $R_{\text{sep}} = 2.0$, and MRSDØ′ PDFs. The inset shows the cross section on a logarithmic scale. There is good agreement between data and theory over 11 orders of magnitude. The main figure shows the percentage difference between the data (points) and theory. Although agreement is excellent below 200 GeV, an excess of events over these theoretical predictions is observed at high E_T. The best agreement below 200 GeV is with the MRSDØ′ PDF. Other PDFs agree less well, and none show the rise at high E_T observed in the data.

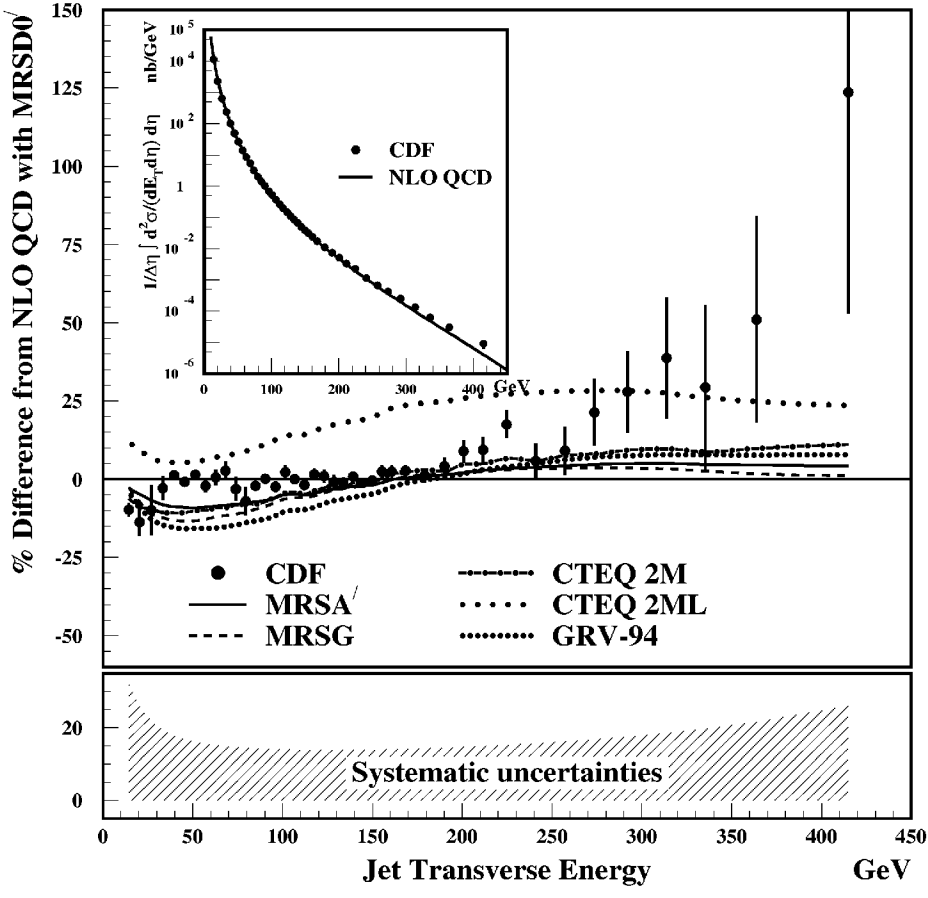

Figure 6 Inclusive jet cross section measured by CDF based on the Run 1A data compared with predictions from the EKS program with $\mu = E_T^{\text{jet}}/2$, $R_{\text{sep}} = 2.0$, and MRSD0′. Error bars represent the statistical uncertainty. The shaded band represents the quadrature sum of the correlated systematic uncertainties. Additional curves show predictions with other parton distribution functions available at the time. For these predictions, the percentage difference relative to the default theory (MRSDØ′) is shown. Inset: the cross section data, from which the comparison with theory is taken.

The systematic uncertainties on the Run 1A cross section were evaluated using the procedures in Reference 45. In short, new parameter sets are derived for ± 1 standard deviation shifts in the unsmearing function for each source of systematic uncertainty. (See Reference 13 for the parameters for the Run 1A cross section.) Figure 7*a–h* shows, for the Run 1A data sample, the percentage change from the standard curve as a function of E_T for the seven largest systematic uncertainties. An eighth uncertainty, an overall normalization uncertainty of $\pm 3.8\%$, was

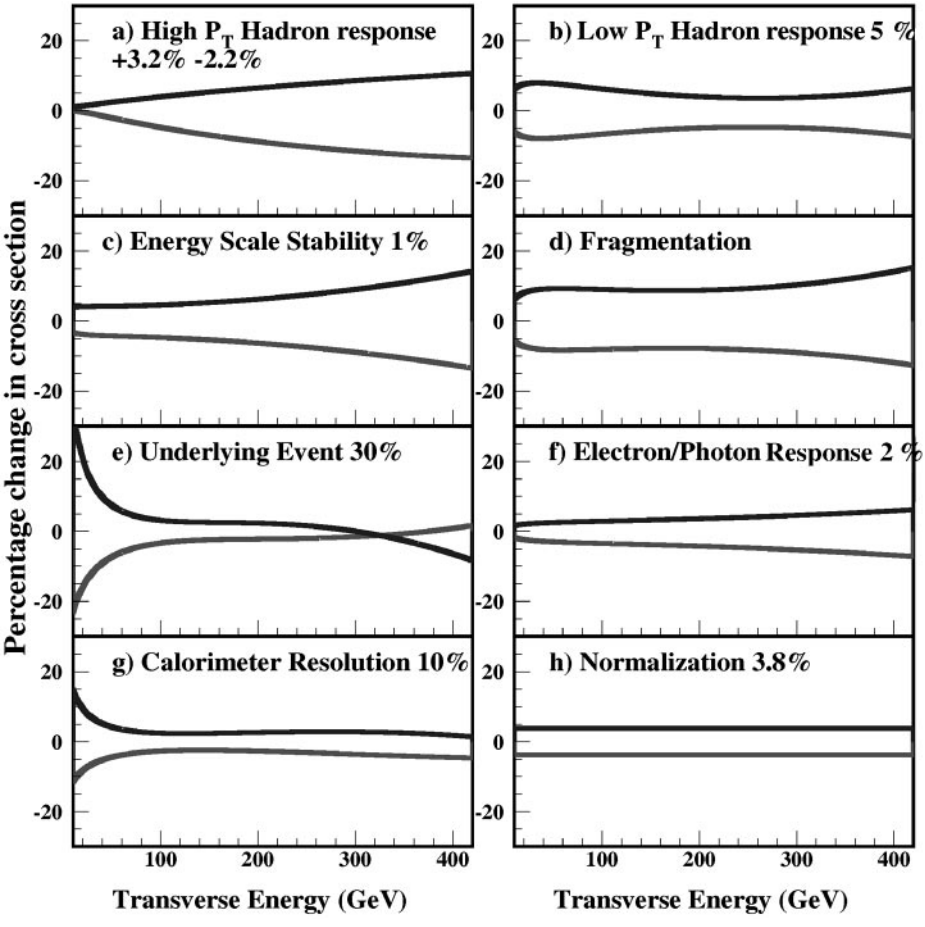

Figure 7 The percentage change in the Run 1A inclusive jet cross section when various sources of systematic uncertainty are changed by ±1 standard deviation from their nominal value. (*a*) Charged hadron response at high P_T; (*b*) the calorimeter response to low-P_T hadrons; (*c*) ±1% on the jet energy for the stability of the calibration of the calorimeter; (*d*) jet fragmentation functions used in the simulation; (*e*) ±30% on the underlying event energy in a jet cone; (*f*) detector response to electrons and photons; (*g*) modeling of the detector jet energy resolution. An eighth uncertainty (*h*), an overall normalization uncertainty of ±3.8%, was derived from the uncertainty in the luminosity measurement (46) (±3.5%) and the efficiency of the acceptance cuts (±1.5%).

derived from the uncertainty in the luminosity measurement (46) ($\pm 3.5\%$) and the efficiency of the acceptance cuts ($\pm 1.5\%$). The eight uncertainties arise from different sources and are not correlated with each other. The 1σ shifts are evaluated by changing only one item at a time in the Monte Carlo simulation, such as high-p_T hadron response. The resulting uncertainty in the unsmeared cross section is thus 100% correlated from bin to bin, but independent of the other seven uncertainties.

To analyze the significance of the Run 1A result, the CDF collaboration used four normalization-independent, shape-dependent statistical tests (13). The eight sources of systematic uncertainty were treated individually to include the E_T dependence of each uncertainty. The effect of finite binning and systematic uncertainties were modeled by a Monte Carlo calculation. Between 40 GeV and 160 GeV, the agreement between data and theory is $>80\%$ for all four tests. Above 160 GeV, however, each of the four methods yields a probability of 1% that the excess is attributable to a fluctuation. If the test is performed for other PDFs, agreement at low E_T is reduced, as is the significance of the excess at high E_T. The best agreement at high E_T for the curves shown is with CTEQ2M (28), which gives 8%, but the low E_T agreement is reduced to 23%.

The excess of events observed at high E_T initiated a reevaluation of the uncertainties in the PDFs, particularly at high x. One outcome of this reexamination was CTEQ4HJ. This PDF incorporates the same low-energy DIS data as CTEQ4M, but the high-E_T jet data are weighted to accentuate its contribution to the global parton distribution fit in the high Q and x region.

Figure 8 compares the preliminary Run 1B result (47) with the Run 1A results and with CTEQ4M (a more modern PDF than those shown in Figure 6). The Run 1A and 1B data sets are in excellent agreement. Only statistical uncertainties are shown. The greatly reduced statistical error bars on the Run 1B data are due to the fivefold increase of luminosity between the two runs. Analysis of the Run 1B data exactly follows the sequence of the Run 1A data with some additional corrections specific to the Run 1B running conditions. The Run 1B systematic uncertainties are very similar to the uncertainties derived for the Run 1A sample. Figure 9 compares the Run 1B result with predictions using other recent PDFs. Although CTEQ4HJ is a bit contrived, the good agreement with the data demonstrates the flexibility of the PDFs and the ability of the QCD calculations to describe these Run 1A and Run 1B inclusive jet cross sections. Quantitative comparisons between the Run 1B data and theoretical predictions are under way.

4.3 The DØ Cross Section

In 1998, the DØ collaboration finalized a measurement of the inclusive jet cross section (18) based on 92 pb^{-1} of data. The DØ analysis differs from the CDF analysis in that the spectrum is corrected independently for energy calibration and then for distortion from finite jet energy resolution. After passing the various jet and event selection criteria, each jet is corrected individually for the average response of the calorimeter. As mentioned in Section 3, the jet response was

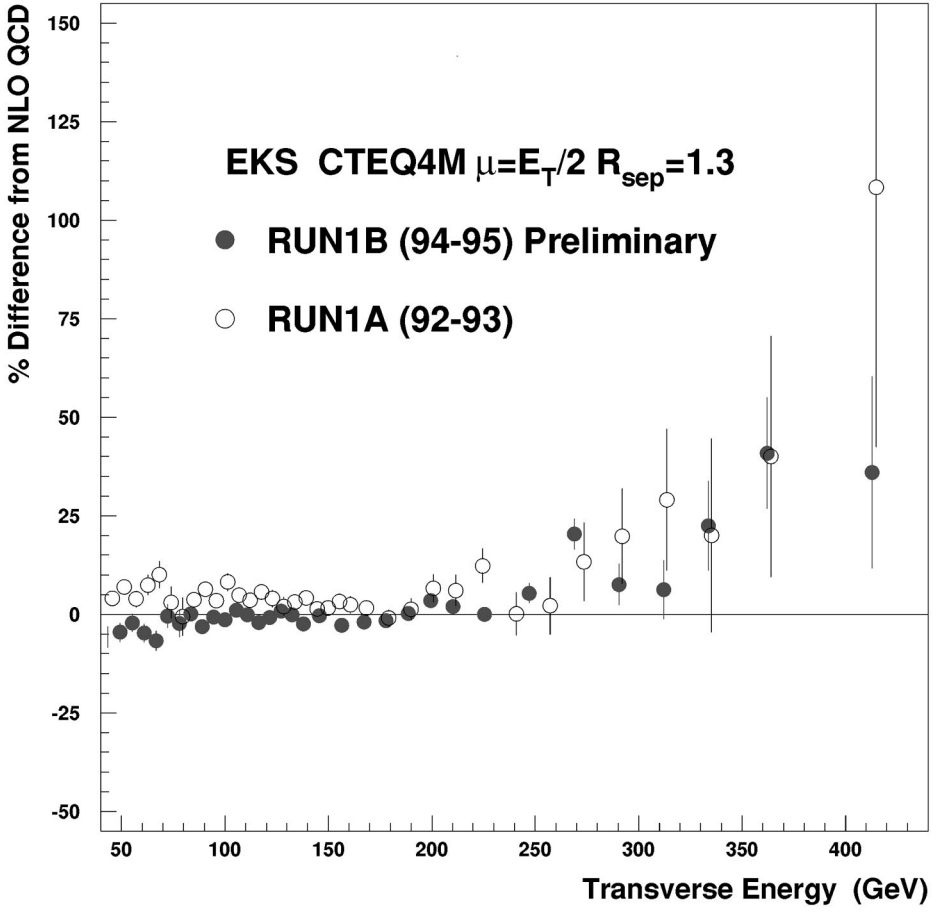

Figure 8 The preliminary Run 1B inclusive jet cross section compared with the published Run 1A data and compared with a QCD prediction from the EKS program with $\mu = E_T^{\text{jet}}/2$, $R_{\text{sep}} = 1.3$, and CTEQ4M.

determined with well-measured photon-jet events. However, the background-free, energy-corrected E_T spectrum still remains distorted by jet energy resolution. The distortion is corrected by first assuming that an Ansatz function $(AE_T^{-B}) \cdot (1 - 2E_T/\sqrt{s})^C$ will describe the actual E_T spectrum, then smearing it with the measured resolution, and finally comparing the smeared result with the measured cross section. The procedure is repeated by varying parameters *A*, *B*, and *C* until the best fit is found between the observed cross section and the smeared trial spectrum. At all E_T, the resolution (measured by balancing E_T in jet events) is well described by a Gaussian distribution; at 100 GeV the standard deviation is 7 GeV. The ratio of the initial ansatz to the smeared ansatz is used to correct the

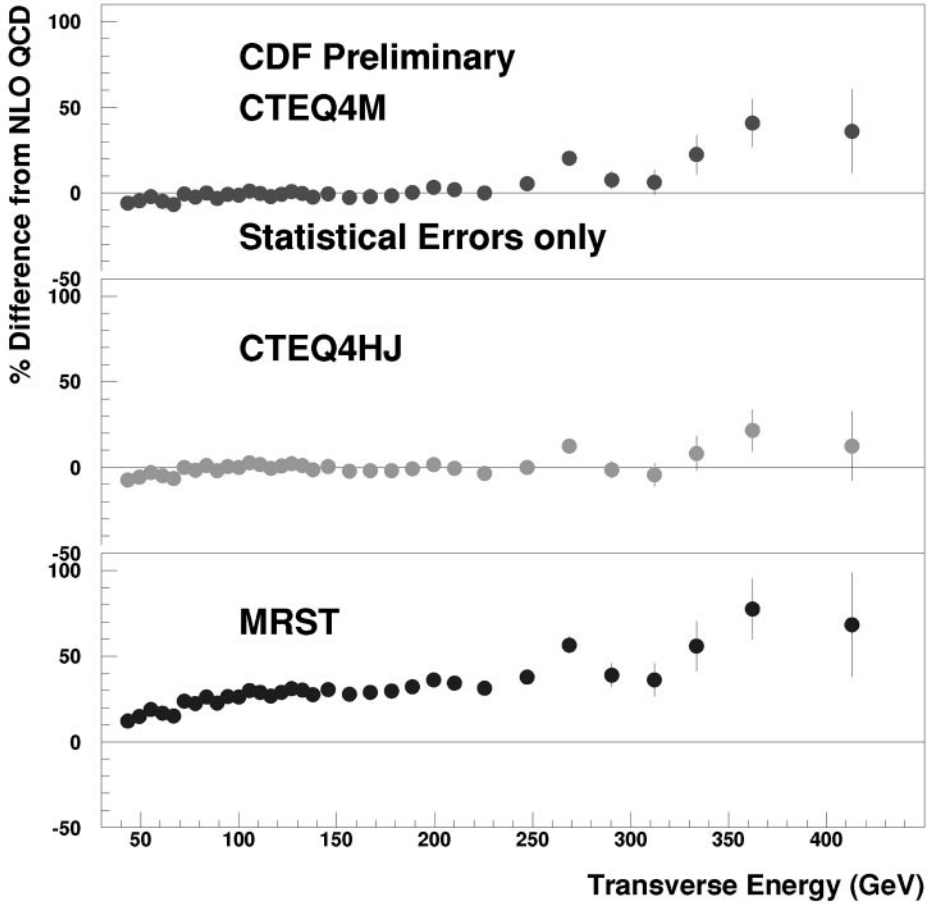

Figure 9 The percent difference between the preliminary Run 1B inclusive jet cross section and QCD predictions from the EKS program with $\mu = E_T^{\text{jet}}/2$, $R_{\text{sep}} = 1.3$, and a variety of current parton distribution functions.

cross section on a bin-by-bin basis (M Bhattacharjee, unpublished thesis). The resolution correction reduces the observed cross section by $(13 \pm 3)\%$ [$(8 \pm 2)\%$] at 60 GeV [400 GeV].

Figure 10 shows the final inclusive jet cross section as measured by the DØ collaboration in the rapidity region $|\eta| \leq 0.5$ (18). This rapidity interval is chosen because the detector is uniformly thick (seven or more interaction lengths with no gaps) and both jet resolution and calibration are precise. The figure shows a theoretical prediction for the cross section from JETRAD. There is good agreement over seven orders of magnitude. For the calculation shown here, $\mu = 0.5E_T^{\max}$, the PDF is CTEQ3M, and $R_{\text{sep}} = 1.3$.

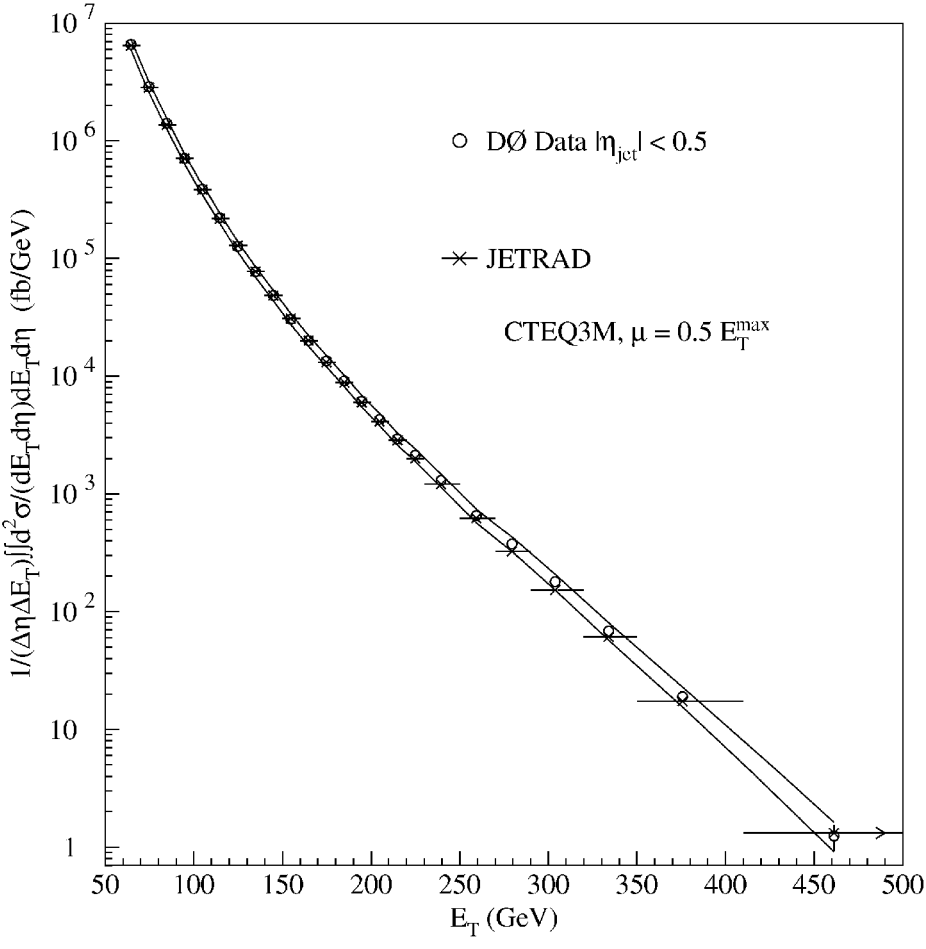

Figure 10 DØ's inclusive cross section at 1800 GeV, $|\eta| \leq 0.5$. Statistical uncertainties are too small to be visible on this scale. The solid curves represent the $\pm 1\sigma$ systematic uncertainty band on the data.

Figure 11 shows the cross-section uncertainties. Each curve represents the average of nearly symmetric upper and lower uncertainties. The energy scale uncertainty, which varies from 8% at low E_T to 22% at 400 GeV, dominates all other sources of uncertainty, except at low E_T, where the 6.1% luminosity uncertainty is of comparable magnitude. The total systematic error is 10% at 100 GeV and 23% at 400 GeV. Although the individual errors are independent of one another, each error is either 100% or nearly 100% correlated point to point, and the overall systematic uncertainty is highly correlated. Table 1 shows that the bin-to-bin correlations in the full uncertainty for representative E_T bins are greater than

TABLE 1 DØ Inclusive jet cross-section total uncertainty correlations

E_T (GeV)	64.6	104.7	204.8	303.9	461.1
64.6	1.00	0.96	0.85	0.71	0.40
104.7	0.96	1.00	0.92	0.79	0.46
204.8	0.85	0.92	1.00	0.91	0.61
303.9	0.71	0.79	0.91	1.00	0.67
461.1	0.40	0.46	0.61	0.67	1.00

40% and positive. The high degree of correlation will prove a powerful constraint on comparisons of the data with the theory.

Figure 12 shows the ratios $(D - T)/T$ for the DØ data (D) and JETRAD NLO theoretical predictions (T) based on the CTEQ3M, CTEQ4M, and CTEQ4HJ for the region $|\eta| \leq 0.5$. Figure 13 shows the same ratios for the $0.1 \leq |\eta| \leq 0.7$ data. Given the experimental and theoretical uncertainties, the predictions are in agreement with the data; in particular, the data above 350 GeV show no indication

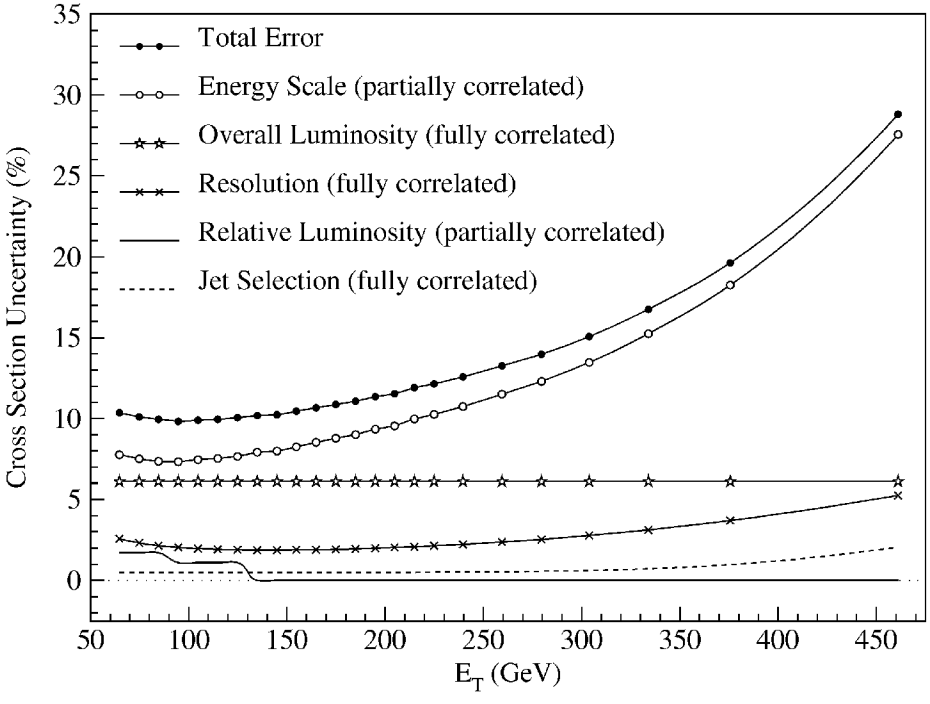

Figure 11 Contributions to the DØ cross section uncertainty for $|\eta| \leq 0.5$.

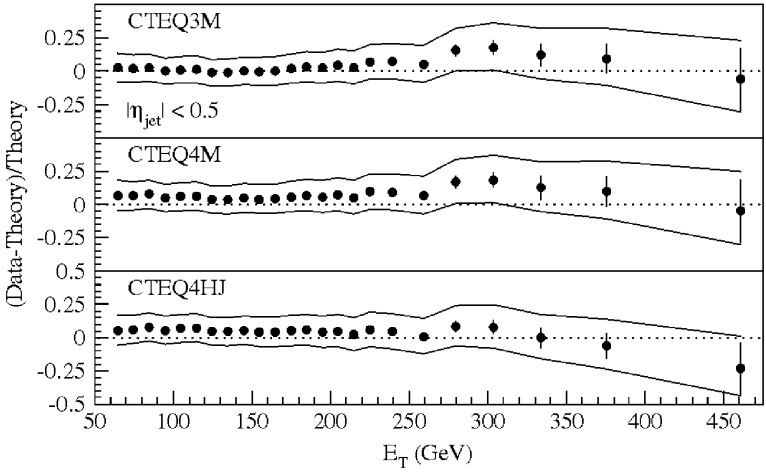

Figure 12 Difference between DØ data and JETRAD QCD predictions with $R_{sep} = 1.3$ and $\mu = E_T^{max}/2$ normalized to predictions for the range $|\eta| < 0.5$. The bands represent the total experimental uncertainty.

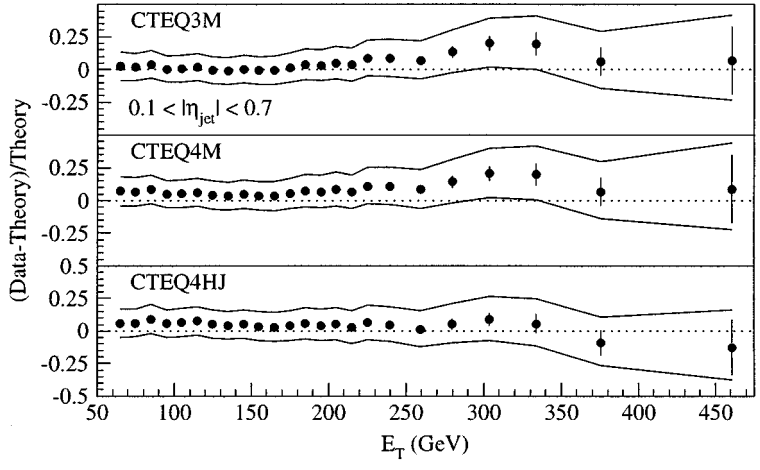

Figure 13 Difference between DØ data and JETRAD QCD predictions with $R_{sep} = 1.3$ and $\mu = E_T^{max}/2$ normalized to predictions for the range $0.1 < |\eta| < 0.7$. The bands represent the total experimental uncertainty.

TABLE 2 χ^2 comparisons between DØ data and JETRAD QCD predictions with $\mu = 0.5E_T^{\max}$, $R_{\text{sep}} = 1.3$, and various PDFs for $|\eta| \leq 0.5$ and $0.1 \leq |\eta| \leq 0.7$ data. There are 24 degrees of freedom

PDF	$\|\eta\| \leq 0.5$	$0.1 \leq \|\eta\| \leq 0.7$
CTEQ3M	23.9	28.4
CTEQ4M	17.6	23.3
CTEQ4HJ	15.7	20.5
MRSA′	20.0	27.8
MRST	17.0	19.5

of a discrepancy relative to QCD. The DØ collaboration has quantitatively compared the data and theory by means of a χ^2 test, incorporating the covariance error matrix. The matrix elements are constructed by analyzing the mutual correlation of the uncertainties in Figure 11 at each pair of E_T values. Table 2 lists χ^2 values for several JETRAD predictions incorporating various PDFs. Each comparison has 24 degrees of freedom. The JETRAD predictions have been fit to a smooth function of E_T. All five predictions describe the $|\eta| \leq 0.5$ cross section very well (the probabilities that χ^2 exceeds the listed values are between 47% and 90%). A similar measurement in the $0.1 \leq |\eta| \leq 0.7$ interval is also well described (probabilities between 24% and 72%). The probabilities calculated by comparing the data with EKS predictions for $\mu = (0.25, 0.5, 1.0) \times E_T^{\max}$ and $\mu = (0.25, 0.5, 1.0) \times E_T^{\text{jet}}$ are all greater than 57%. Perturbative QCD is in good agreement with the data with or without large x enhancements to the PDFs.

4.4 Comparison of the CDF and DØ Measurements

The two inclusive jet analyses differ in an important but complementary way. The CDF analysis uses a Monte Carlo program carefully tuned to collider and test-beam data, in order to correct for detector response. In contrast, DØ corrects for calorimeter response by direct utilization of collider data. Both collaborations invested a great deal of time and effort in developing these procedures. The CDF technique capitalizes on the excellent tracking capabilities of the detector. The tracking is used to directly measure the jet fragmentation functions as well as to verify test-beam calibrations of the calorimeter modules. Additional checks of the Monte Carlo simulation come from comparisons of jet E_T balancing in jet events. The uniformity of the DØ calorimetry permits a precise collider-based measurement of jet response and resolution at all energies and rapidities. This uniformity permits transfer of the jet energy calibration at low to moderate jet energies in the central calorimeter to all pseudorapidity with a missing E_T technique.

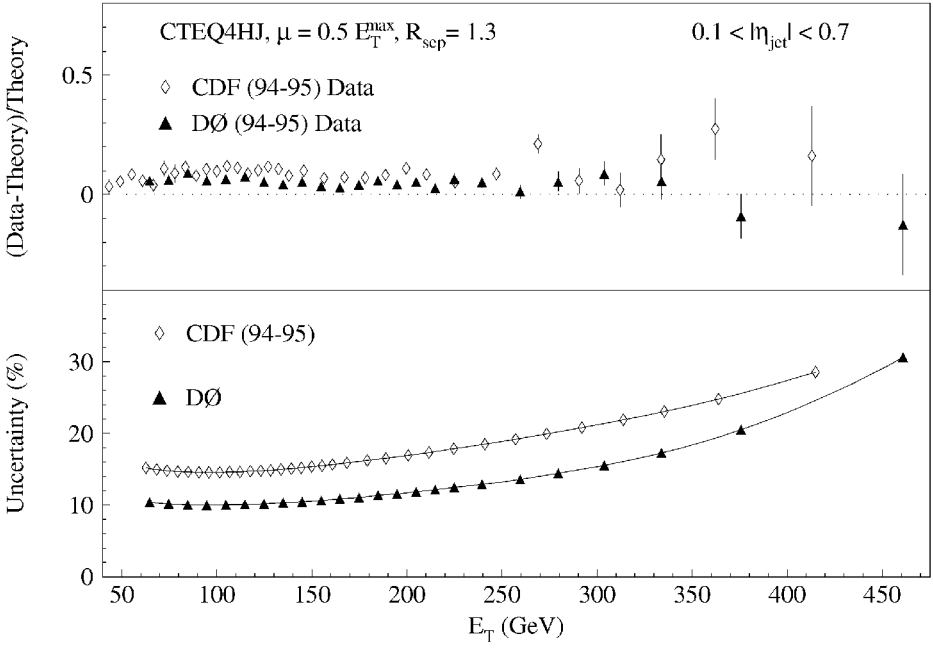

Figure 14 *Top*, comparisons of DØ and CDF data to JETRAD in the region $0.1 < |\eta| < 0.7$. *Bottom*, the quadrature sums of the DØ and CDF uncertainties.

The forward calorimetry provides an opportunity for direct calibration of high-energy jets relative to these central photons. The uniformity, linearity, and depth of the detector also assures that resolution functions are relatively narrow and Gaussian.

The top half of Figure 14 shows $(D-T)/T$ for the Run 1B DØ and CDF data sets in the $0.1 \leq |\eta| \leq 0.7$ region relative to a JETRAD calculation using CTEQ4HJ, $\mu = 0.5E_T^{\max}$, and $R_{\rm sep} = 1.3$. Note that there is outstanding agreement for $E_T \leq 350$ GeV. At higher E_T the two results diverge but not significantly given the statistical and systematic errors. This impression is fortified by a direct comparison of the magnitude of the DØ and CDF uncertainties, as shown in the bottom half of the figure. To quantify the degree of agreement, the DØ collaboration has carried out a χ^2 comparison between their data and the nominal curve describing the central values of the CDF Run 1B data. The nominal curve is used instead of the data points because each of the measurements reports the cross section at different values of jet E_T. Comparison of the DØ data to the nominal Run 1B curve yields a χ^2 of 41.5 for 24 degrees of freedom. A statistical error-only comparison of the DØ and CDF data is approximated by calculating the value of the CDF curve at the DØ E_T points and assuming that the statistical uncertainty on the CDF and

DØ data are equivalent (the DØ statistical errrors are multiplied by $\sqrt{2}$.) When the 2.7% relative normalization difference (37) is removed, the χ^2 based on statistical error only is 35.1 for 24 degrees of freedom, a probability of 5.4%. When the systematic uncertainties in the covariance matrix are expanded to include both the DØ and CDF uncertainties and the DØ statistical errors are increased by $\sqrt{2}$, the χ^2 equals 13.1, corresponding to a probability of 96%.

Considering the complexities of these analyses, the overall agreement is remarkable. Given the present flexibility of the PDFs and the mixed agreement between the data and theory at the highest x and Q, no clear indication of a high-E_T deviation with QCD can be inferred. By using the high-E_T jet data, PDFs can be derived that describe both data sets. An unambiguous search for deviations, however, requires an independent measure of the PDFs. Prospects for improvements to the PDFs are covered in later sections. First we turn to inclusive jet measurements at a different beam energy.

5. RATIO OF JET CROSS SECTIONS AT TWO BEAM ENERGIES

5.1 Inclusive Jet Cross Sections, Scaling, and the Ratio of Dimensionless Cross Sections

An alternative test of QCD compares the inclusive jet cross sections measured at widely separated center-of-mass energies. The hypothesis of "scaling" predicts that the dimensionless, scaled jet cross section,

$$E_T^4 (E d^3\sigma/dp^3),$$

will be independent of $\sqrt{s}$ as a function of the dimensionless variable $x_T = 2E_T/\sqrt{s}$. This can be written in terms of the experimentally measured quantities as

$$\sigma_d = \left(E_T^3/2\pi\right) d^2\sigma/dE_T\, d\eta.$$

QCD predictions depend on the energy scale, or Q^2, of the interactions and thus suggest that the cross sections should not scale. The energy dependence of the strong coupling and the evolution of the PDFs are manifestations of this energy (or scale) dependence of the predictions.

Measurement of the ratio of the scaled jet cross sections from two different center-of-mass energies (in the same experimental apparatus) provides a test of QCD in which many theoretical and experimental uncertainties cancel. Figure 15 shows the ratio of the scaled cross sections, $\sigma_d^{630}/\sigma_d^{1800}$, calculated with JETRAD. The top two panels show a 10% variation in the ratio below $x_T = 0.4$ (jet $E_T =$ 360 GeV at $\sqrt{s} = 1800$ GeV) because of the choice of scale. The bottom two panels demonstrate that PDF choices produce variations below 10%.

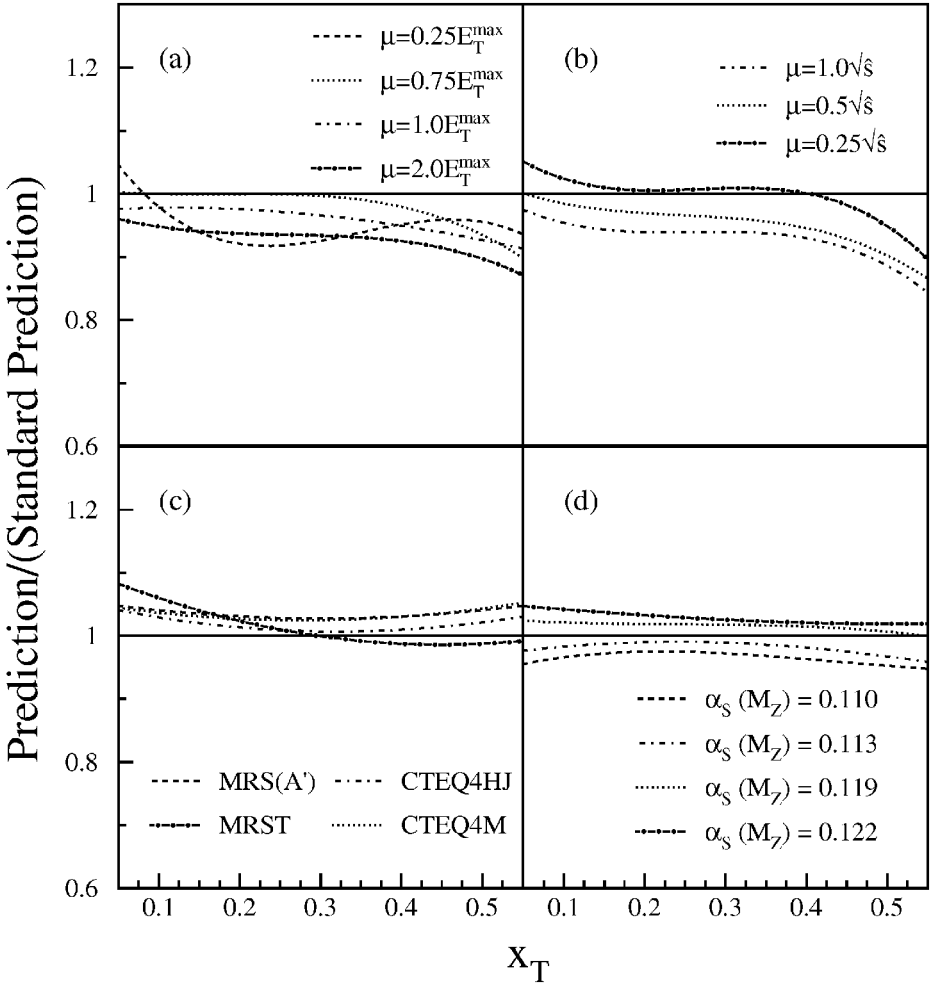

Figure 15 The difference between other predictions and the reference prediction ($\mu = 0.5E_T^{\max}$, CTEQ3M) of the ratio of inclusive jet cross sections at $\sqrt{s} = 630$ GeV and 1800 GeV for $\eta_{\text{jet}} \leq 0.5$. The other predictions are for the choices (*a*) $\mu = 0.25$, 0.75, 1.0, and $2.0 \times E_T^{\max}$, (*b*) $\mu = 0.25$, 0.5, and $1.0 \times \sqrt{s}$, (*c*) CTEQ4M, CTEQ4HJ, MRS(A′), and MRST, and (*d*) calculations with the CTEQ4A series of PDFs (which vary α_s) compared with the calculation using CTEQ4M.

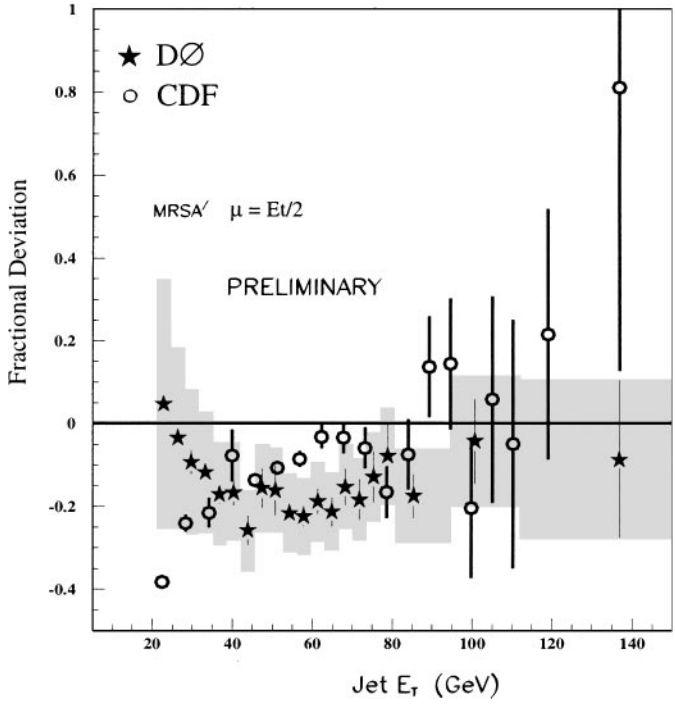

Figure 16 Preliminary DØ and CDF $\sqrt{s} = 630$ GeV cross-section data compared with next-to-leading-order QCD predictions. The shaded area represents the DØ systematic errors.

5.2 Jet Production at 630 GeV

In December 1995, CDF and DØ each collected $\approx 600\,\text{nb}^{-1}$ of data at $\sqrt{s} = 630$ GeV (beam energies of 315 GeV). A primary motivation was to test whether the inclusive jet cross section at this reduced energy and the ratio relative to 1800 GeV would shed light on the deviations seen in the Run 1A data. The analysis of the 630-GeV data follows a path identical to that of the analysis described above for the 1800-GeV data. Figure 16 shows the preliminary measurements from CDF (48) and DØ (49) of the inclusive cross section at $\sqrt{s} = 630$ GeV. The CDF measurement is for the region $0.1 \leq |\eta| \leq 0.7$, whereas the DØ result is for the region $|\eta| \leq 0.5$. The figure shows the percent difference between the data and the associated theory prediction. The NLO theoretical predictions used the MRSA′ PDF and $\mu = 0.5E_T^{\text{jet}}$. The two measurements are in agreement above 80 GeV, but some discrepancy exists near and below 60 GeV. The discrepancies are within the 20–30% systematic uncertainties reported by DØ and represented by the shaded boxes. The predicted cross section is larger, though not significantly, than the measured cross section for E_T less than 80 GeV. Note that in this E_T range, results at $\sqrt{s} = 1800$ GeV show good agreement between data and theoretical predictions.

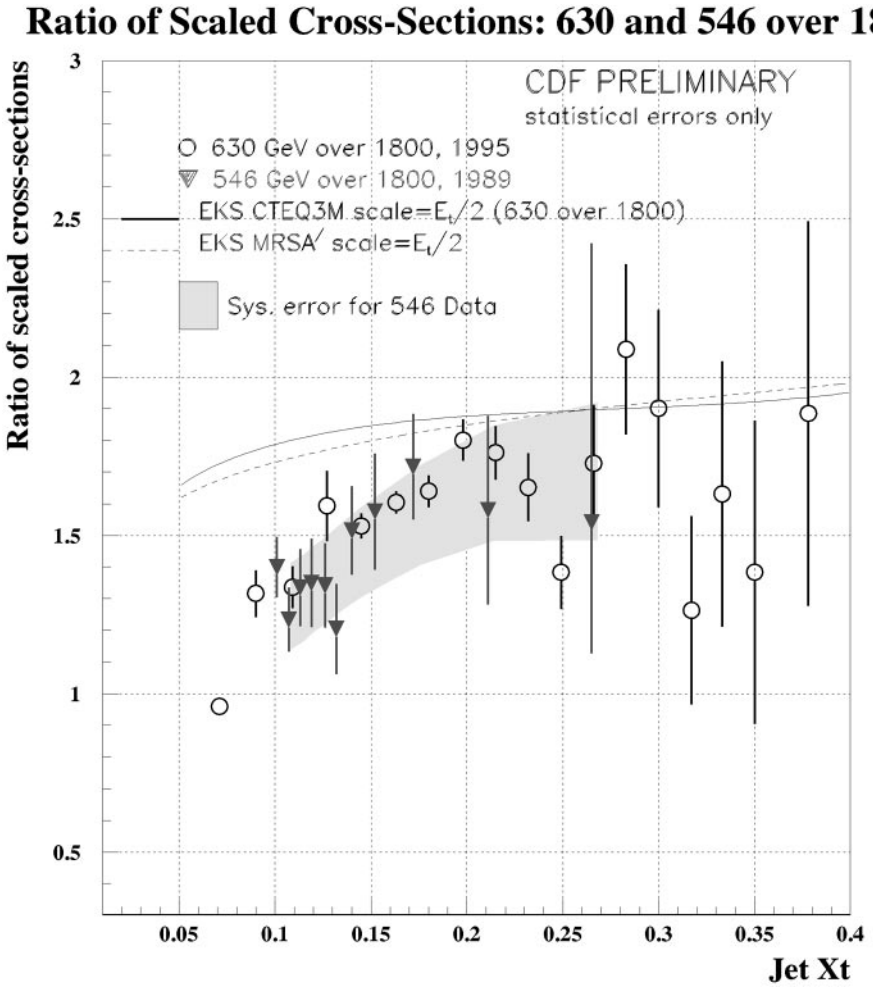

Figure 17 CDF scaling result from Tevatron runs at $\sqrt{s} = 546$ GeV and 1800 GeV in 1989, compared with the preliminary result from the Run 1B runs at 630 GeV and 1800 GeV.

5.3 The Scaled Cross Sections

Figure 17 shows the preliminary ratio of the scaled cross sections (48) from CDF, $\sigma_d^{630}/\sigma_d^{1800}$, along with the previous CDF result (45) for $\sigma_d^{546}/\sigma_d^{1800}$ from much smaller data samples. The shaded band indicates the systematic uncertainty on the 546/1800 ratio; the uncertainties on the 630/1800 GeV ratio are similar, but their analysis is not yet final. The results agree well. The 546-GeV result ruled out scaling at the 95% confidence level, and a disagreement with QCD predictions was observed at low E_T.

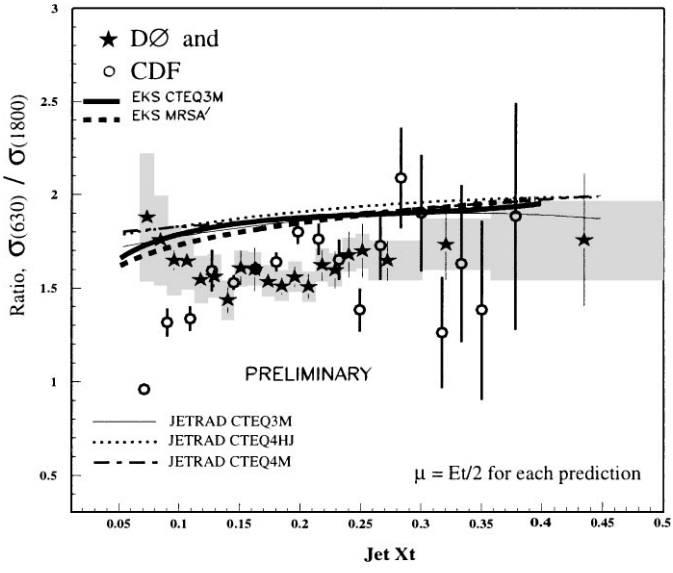

Figure 18 Preliminary DØ and CDF cross-section ratios for $\sqrt{s} = 630$ GeV to $\sqrt{s} = 1800$ TeV compared with next-to-leading-order QCD predictions. The shaded area represents the DØ systematic errors.

Figure 18 shows the preliminary cross-section ratios from DØ (49) and CDF compared with a variety of theoretical predictions. Many of the energy-scale and luminosity uncertainties cancel in the ratio. The uncertainty on the DØ ratio, shown by the shaded area, is about 7%, much less than the 15–30% uncertainty on the cross sections, and about a factor of two better than previous ratio measurements. The CDF and DØ ratios are consistent with each other for $x_T \geq 0.1$, but some difference may exist for $x_T \leq 0.1$. The discrepancy between the two measured ratios reflects the discrepancy in Figure 16. The significance of the difference must await completion of the analysis of the CDF systematic uncertainties. The predicted ratio is roughly 20% higher than the ratio measured by DØ. Figure 18 also shows three NLO QCD JETRAD predictions for the ratio using $\mu = 0.5E_T^{\max}$, $R_{\text{sep}} = 1.3$, and different PDFs. In addition, two NLO predictions from the EKS program using CTEQ3M and MRSA′ and $\mu = 0.5E_T$ are shown. Notice that the variation in the predicted ratios is very small.

The preliminary inclusive jet cross sections at $\sqrt{s} = 630$ GeV are not well described by NLO QCD calculations. Quantitative results on these comparisons await determination of final experimental uncertainties. The ratio of inclusive cross sections is also in mild disagreement with the theory. With a larger data sample, these measurements could place constraints on the high-x behavior of the PDFs while using relatively low E_T jets. An additional run at a similar beam energy should be considered for Run 2. We now turn to a different technique of probing

high-x behavior, namely the study of the correlations between the leading two jets resulting from a $p\bar{p}$ collision.

6. DIJET DIFFERENTIAL CROSS SECTIONS AT LARGE RAPIDITY

6.1 Introduction

Measurements of the dijet differential cross sections in different rapidity regions can provide additional information and constraints on the QCD predictions. Restricting the E_T and rapidity of the leading two jets in the events allows different regions of x and Q^2 to be probed. This may permit a more direct measure of the proton PDFs at Tevatron energies. For instance, at LO, a jet with $E_T = 90$ GeV and $\eta = 0$ ($\theta = 90^\circ$) must be balanced by a second jet with $E_T = 90$ GeV. If the second jet is at $\eta = 0$, both jet energies equal 90 GeV, so $x_1 = x_2 = 0.10$. However, if the second jet is more forward, $\sin\theta$ is smaller, and the jet energy ($E = E_T/\sin\theta$) and its fraction of the initial hadronic momentum must increase to maintain $E_T =$ 90 GeV. At LO, the parton momentum fraction x is related to the E_T and η of the two jets by the following equations:

$$x_1 = \frac{E_T}{\sqrt{s}}(e^{\eta_1} + e^{\eta_2}), \quad x_2 = \frac{E_T}{\sqrt{s}}(e^{-\eta_1} + e^{-\eta_2}).$$

For $E_T = 90$ GeV at $\eta = 0$ and 2, the fractional energies are $x = 0.06$ and 0.42. For multijet production, the calculations of x are generalized to

$$x_1 = \frac{1}{\sqrt{s}}\sum_i E_{Ti}e^{\eta_i}, \quad x_2 = \frac{1}{\sqrt{s}}\sum_i E_{Ti}e^{-\eta_i},$$

where i runs over all jets in an event.

Experimentally, the differential dijet cross sections are most conveniently given by

$$\frac{d^3\sigma}{dE_T d\eta_1 d\eta_2},$$

where η_1 and η_2 are the pseudorapidities of the leading two jets. Like the inclusive cross section, the dijet differential cross sections are integrated over a range of pseudorapidity. The cross sections are also integrated over a range of E_T, but here there is even more freedom in the definition of E_T—the leading jet E_T, the average of the leading two jet E_Ts, or both leading jet E_Ts (two entries into the cross section, one for the E_T of each of the leading two jets). The choice depends on the experimental conditions. Although they are still preliminary, we present the dijet differential cross sections here in order to demonstrate the potential and strength of these measurements. Once the systematic uncertainties are well understood, these measurements will strongly constrain the PDFs.

6.2 The CDF Measurement

In the CDF Run 1B measurement, the two highest E_T jets are identified and one is required to be in the central ($0.1 \leq |\eta| \leq 0.7$) region. Because the central region has the smallest energy-scale uncertainty, the central jet is used to measure the E_T of the event. The other jet, called the probe jet, is required to have $E_T > 10$ GeV and to fall in one of the η bins: $0.1 \leq |\eta| \leq 0.7$, $0.7 \leq |\eta| \leq 1.4$, $1.4 \leq |\eta| \leq 2.1$, or $2.1 \leq |\eta| \leq 3.0$. There are no restrictions on the presence of additional jets. Figure 19 shows the preliminary cross section (47) in the individual η bins as a function of the central jet E_T. JETRAD is used for the theoretical predictions with scale $\mu = 0.5E_T^{\max}$ and $R_{\text{sep}} = 1.3$. The data are compared to the predictions using three PDFs: CTEQ4HJ, MRST, and CTEQ4M. The statistical uncertainty is shown on the points. Figure 20 shows the percent difference between the data and theory (CTEQ4M) as a function of the central jet E_T for each rapidity bin. The additional curves represent the percent difference between the predictions with CTEQ4M and predictions using MRST and CTEQ4HJ. The systematic uncertainty on the

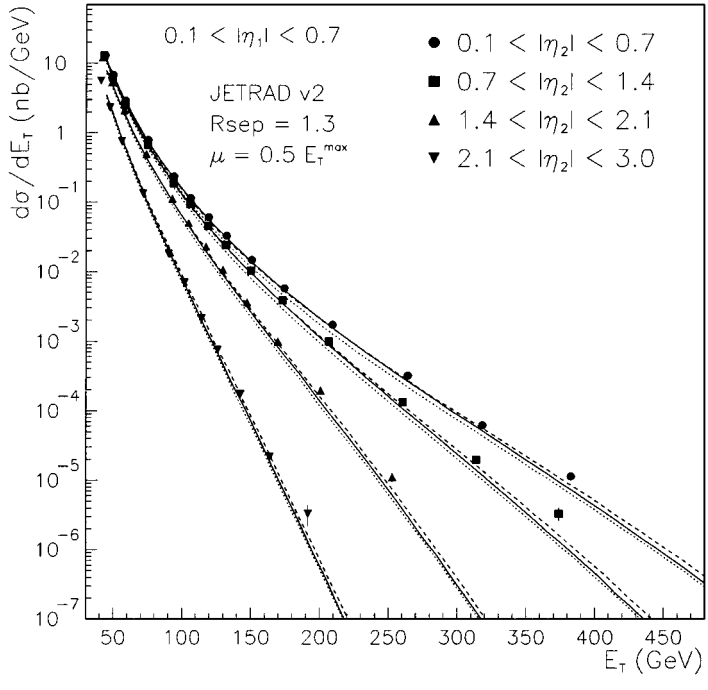

Figure 19 Preliminary CDF cross sections for central jets ($0.1 \leq |\eta| \leq 0.7$) with the second jet in different rapidity intervals. Solid line, CTEQ4M; dashed line, CTEQ4HJ; dotted line, MRST.

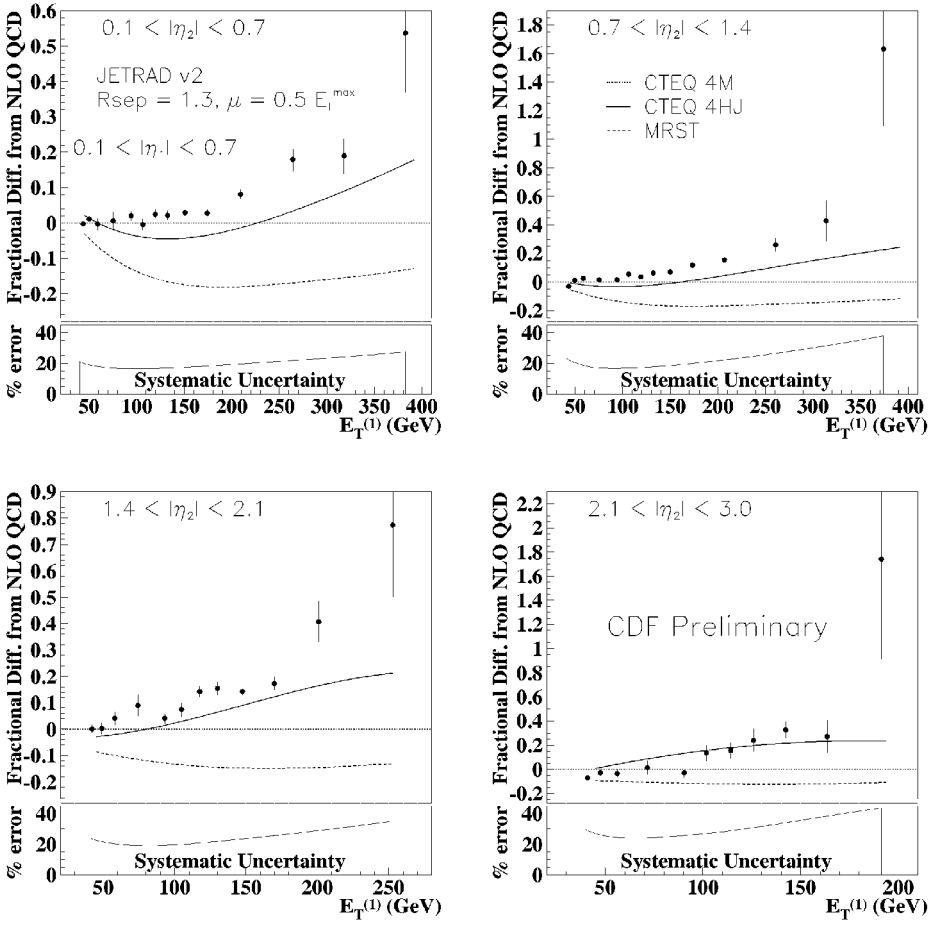

Figure 20 Percent difference between preliminary CDF data (points) and a next-to-leading-order QCD prediction using the JETRAD program, CTEQ4M, $R_{\text{sep}} = 1.3$, and $\mu = E_T^{\max}/2$. The percent difference between predictions using CTEQ4M and predictions using MRST and CTEQ4HJ are also shown. The four plots represent the cross section as a function of the central jet E_T when the rapidity of the second jet is restricted to different ranges. The curve in the lower box represents the quadrature sum of the correlated systematic uncertainties.

measurement is evaluated in a manner similar to the uncertainty on the inclusive jet cross section. The quadrature sum of the systematic uncertainties is shown in the box below the points. The high rapidity bins reach x of roughly 0.6–0.7, while the E_T of the jets is in the 100–200 GeV range. As in the inclusive cross section measurement, the dijet differential cross section shows an excess at high E_T over predictions using CTEQ4M. The presence of this excess in all four rapidity bins suggests that this difference is not a function of the jet E_T, but rather a function

TABLE 3 x Ranges of same-side (SS) and opposite-side (OS) dijet differential cross sections

η bin	Topology	$x_{\min}$	$x_{\max}$
0.0–0.5	SS	0.04	0.53
0.0–0.5	OS	0.07	0.42
0.5–1.0	SS	0.03	0.73
0.5–1.0	OS	0.08	0.45
1.0–1.5	SS	0.02	0.81
1.0–1.5	OS	0.10	0.44
1.5–2.0	SS	0.01	0.80
1.5–2.0	OS	0.16	0.46

of x and is thus related to inadequacies in the PDFs. The improved agreement in all bins when CTEQ4HJ is used is similarly suggestive.

6.3 The DØ Measurement

The DØ Run 1B (92 pb^{-1}) measurement organizes the dijet differential cross section according to the rapidity of both leading jets. The rapidities are divided into four same-side (SS) bins where $\eta_1 \sim \eta_2$ and four opposite-side (OS) bins where $\eta_1 \sim -\eta_2$. Table 3 lists the bins and approximated x ranges sampled (assuming a L0 process and the observed E_T ranges in each bin). The eight cross sections are all plotted versus jet E_T. Here each event has two entries, one for the E_T of each of the leading two jets. As indicated in the table, the low rapidity measurements can provide confirmation of previous PDF measurements extrapolated from low Q^2. On the other hand, the large-rapidity SS events probe much larger x values.

The DØ analysis follows the inclusive analysis very closely. Jet and event selection, energy correction, and resolution unsmearing are all similar. An additional correction for vertex resolution is also important in the very forward and backward rapidity bins. The cross-section uncertainties are similar to the inclusive cross section for the four rapidity bins limited by $\eta = 1.0$. In the high-η bins the systematic errors are approximately doubled. Figures 21 and 22 show the fractional difference between data and theory for all eight bins (47, 50). The theoretical prediction is from JETRAD with CTEQ3M and $\mu = 0.5E_T^{\max}$. The bars on the data represent the statistical uncertainty and the triangles mark the total uncertainty. There is good agreement over all rapidity for $x = 0.01$ to 0.80. Significantly, this PDF includes no collider jet data. The agreement with CTEQ4M (not shown) is also reasonable.

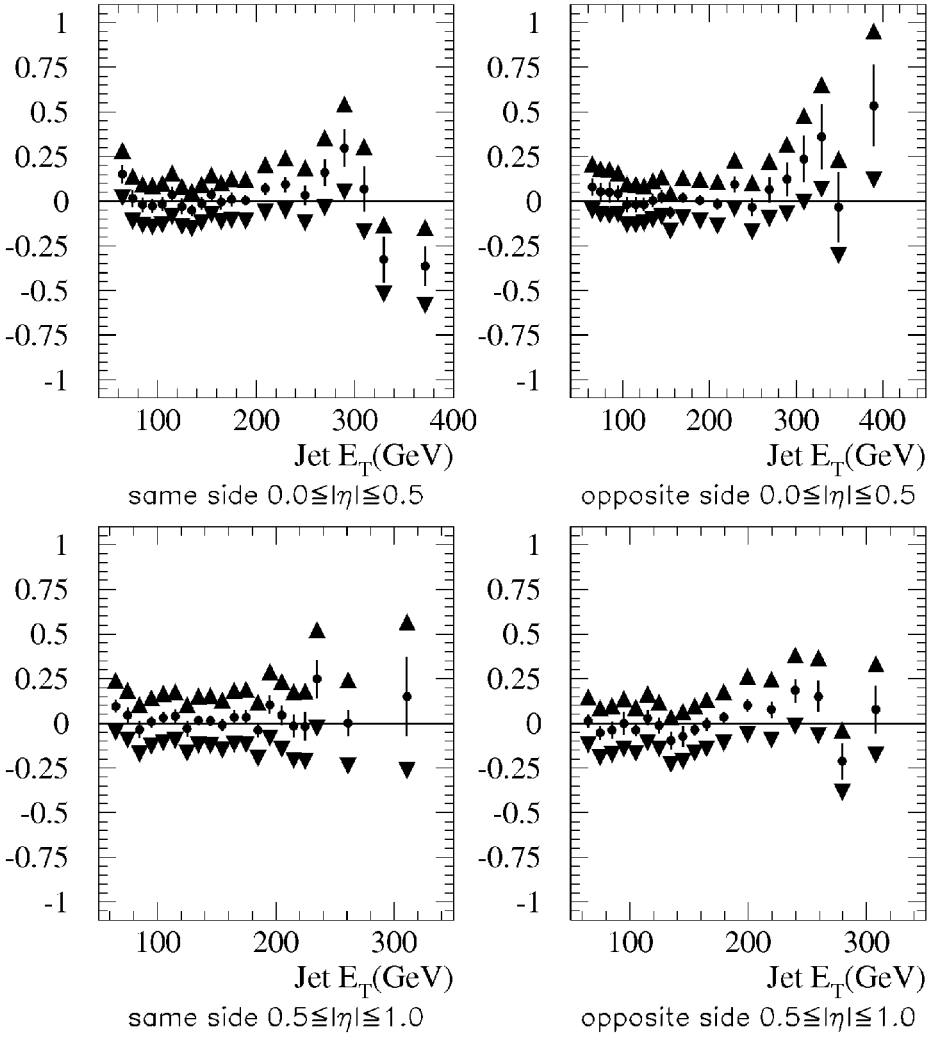

Figure 21 DØ same-side and opposite-side cross sections compared with JETRAD with $R_{\text{sep}} = 1.3$, $\mu = E_T^{\max}/2$, and CTEQ3M. The top plots restrict the rapidity of the two leading jets to absolute rapidities less than 0.5 and the bottom plots to absolute rapidities between 0.5 and 1.0. See the text for details.

6.4 Prospects

The differential cross section data show great promise for constraining the PDFs. In all rapidity bins, the CDF data appear to prefer CTEQ4HJ over CTEQ4M or MRST, whereas the DØ data seem in good agreement with the predictions using CTEQ3M. This apparent disagreement mirrors the situation in the inclusive cross sections. However, a firm statement on the agreement or disagreement of the two

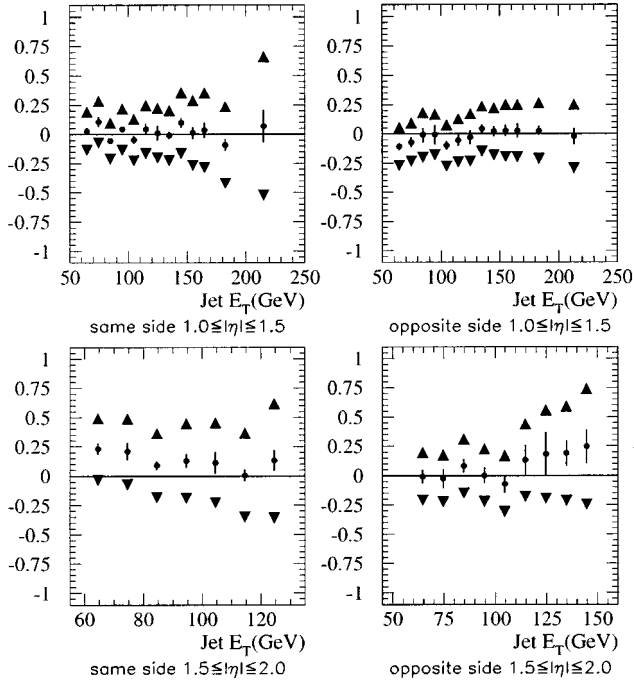

Figure 22 DØ same-side and opposite-side cross sections compared with JETRAD with $R_{\rm sep} = 1.3$, $\mu = E_T^{\rm max}/2$, and CTEQ3M. The top plots restrict the rapidity of the two leading jets to absolute rapidities between 1.0 and 1.5 and the bottom plots to absolute rapidities between 1.5 and 2.0. See the text for details.

data sets is obscured by the different techniques and the current lack of more quantitative comparisons between data and theory.

7. DIJET MASS AND ANGULAR DISTRIBUTIONS AT 1800 GeV

7.1 Introduction

The LO cross section for $p\bar{p} \to jet_1 + jet_2 + X$ events (where jet_1 and jet_2 are the leading two jets) can be completely described in terms of three orthogonal center-of-mass variables. These are $\cos\theta^*$ (where θ^* is the center-of-mass scattering angle between the two leading jets), the boost of the dijet system $\eta_{\rm boost} = (\eta_1 + \eta_2)/2$, and the dijet mass M_{jj}, as follows (51):

$$\frac{d^3\sigma}{d\eta_{\rm boost}\, dM_{jj} d\cos\theta^*} = \frac{\pi\alpha_s^2(Q^2)}{2s^2}(2M_{jj}) \sum_{1,2} \frac{f(x_1, Q^2)}{x_1} \frac{f(x_2, Q^2)}{x_2} |m_{12}|^2,$$

where $\alpha_s(Q^2)$ is the strong coupling strength, $|m_{12}|^2$ is the hard scattering matrix element, $x_1(x_2)$ is the fraction of the proton (antiproton) momentum carried by the parton, and $f(x_1, Q^2)$ is the parton momentum distribution. Typically the dijet mass is derived from measured variables such as E_T, η_{jet}, and ϕ_{jet}. In the case of higher-order processes, where more than two jets are produced, the mass is calculated using the two highest E_T jets in the event and additional jets are ignored.

Integration of the general dijet cross section over boost and production angle results in the dijet mass spectrum. The spectrum is a useful test of QCD sensitive to the PDFs. On the other hand, integration over mass and boost leads to the dijet angular distribution—a marvelous test of the hard scattering matrix elements almost totally insensitive to the PDFs. Comparisons of the angular distributions and certain mass spectra ratios to theoretical predictions can establish stringent limits on the presence of conjectured quark constituents. We now discuss these spectra and compositeness limits.

7.2 The Mass Distributions

At LO, where only two jets are produced, the dijet invariant mass is given by

$$M_{jj}^2 = \hat{s} = x_1 x_2 s,$$

where $\hat{s}$ is the center-of-mass energy of the interacting partons and s is the total center-of-mass energy. Because the dijet mass represents the center-of-mass energy of the interaction, it directly probes the PDFs. Experimentally, the dijet mass cross section is given by

$$\frac{d^3\sigma}{dM_{jj}\, d\eta_1\, d\eta_2},$$

where η_1 and η_2 are the pseudorapidities of the jets. Like the inclusive jet cross section, the dijet mass cross section is integrated over a range of pseudorapidity. For example, Figure 23 shows NLO QCD dijet predictions for $|\eta_{\text{jet}}| \leq 1.0$ relative to a reference prediction. There are 20–30% variations owing to the scale and to the PDFs.

The DØ and CDF collaborations have both measured the dijet mass spectrum with Run 1B data samples. The CDF measurement uses the four-vector definition for the dijet mass $M_{jj} = \sqrt{(E_1 + E_2)^2 - (\vec{P}_1 + \vec{P}_2)^2}$, where E and $\vec{P}$ are the energy and momentum of a jet, and allows the rapidity of the jets to extend to $|\eta_{\text{jet}}| < 2.0$. To ensure good acceptance, the CDF analysis also imposes a cut on $|\cos\theta^*| < 2/3$, where θ^* is the scattering angle in the center-of-mass frame. Figure 24 compares the CDF preliminary data with JETRAD predictions (47). The error bars represent the quadrature sum of the statistical and systematic uncertainties. The data and JETRAD predictions using CTEQ4M, $\mu = 0.5E_T^{\text{jet}}$, and $R_{\text{sep}} = 1.3$ are in good agreement. Figure 25 shows the percent difference between the data and

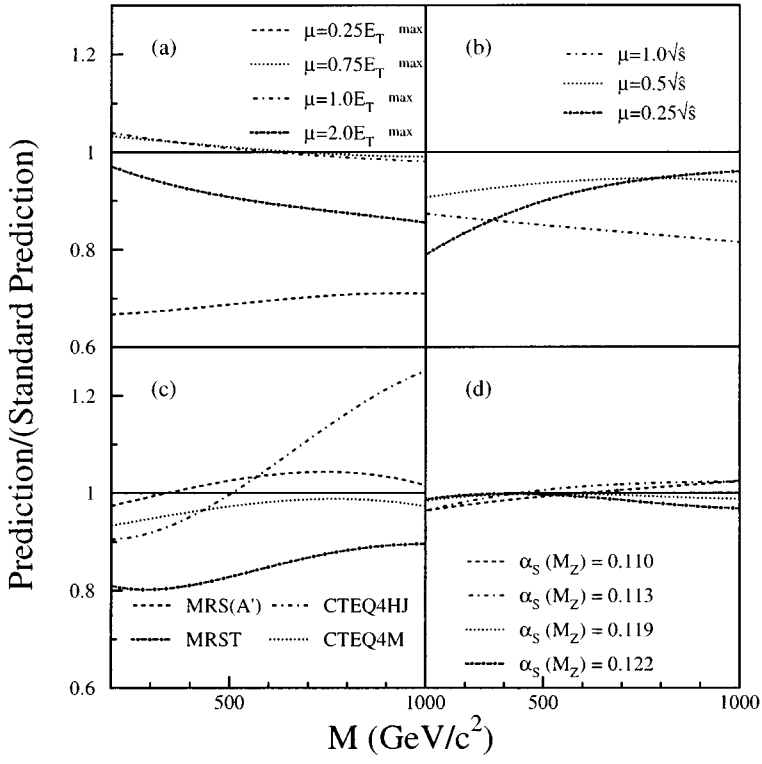

Figure 23 The difference between alternative predictions and the reference prediction ($\mu = 0.5E_T^{\max}$, CTEQ3M) for the inclusive dijet mass cross section at $\sqrt{s} = 1800$ GeV for $\eta_{\text{jet}} \leq 1.0$. The alternative predictions are for (*a*) $\mu = 0.25$, 0.75, 1.0, and $2.0 \times E_T^{\max}$, (*b*) $\mu = 0.25$, 0.5, and $.0 \times \sqrt{s}$, (*c*) CTEQ4M, CTEQ4HJ, MRS(A′), and MRST, and (*d*) calculations with the CTEQ4A series of parton distribution functions (which vary α_s) compared with the calculation using CTEQ4M.

the theoretical prediction. The shaded band shows the preliminary estimate of the systematic uncertainties. These uncertainties are derived in a manner similar to the uncertainties on the inclusive jet cross-section measurement, with additional contributions for jets outside the central region. The percent difference between the default prediction and predictions using other PDFs are all consistent with the data, given the present systematic errors. However, as with the inclusive and dijet cross-section measurements, CTEQ4HJ seems to provide the best agreement with the data in the high-E_T region.

DØ has performed the dijet mass measurement in two rapidity regions: central ($|\eta_{\text{jet}}| < 0.5$) and more forward ($|\eta_{\text{jet}}| < 1.0$, $|\Delta\eta_{\text{jet}}| < 1.6$) (52). The dijet mass at DØ is defined assuming massless jets, $M_{jj} = \sqrt{2E_T^1 E_T^2(\cosh(\Delta\eta) - \cos(\Delta\phi))}$, where $\Delta\eta$ and $\Delta\phi$ are the rapidity and azimuthal separation of the two jets.

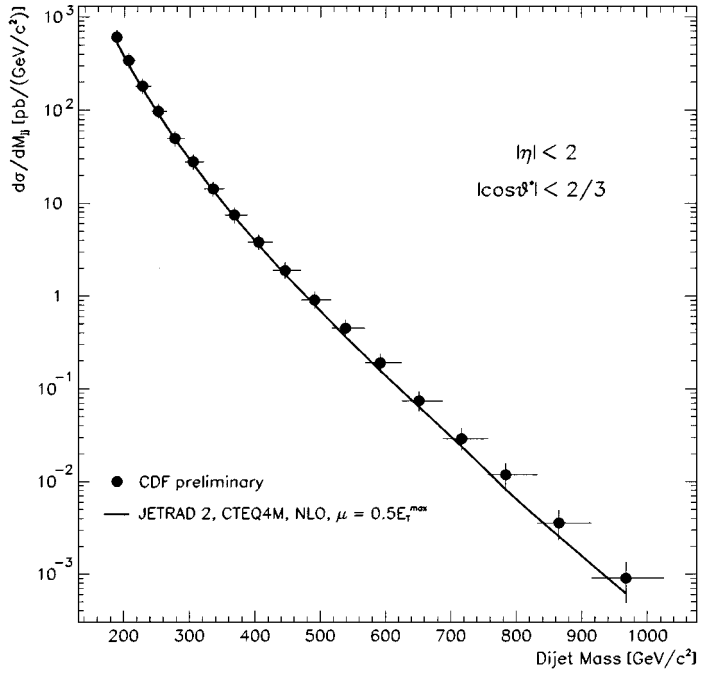

Figure 24 Dijet mass as measured by CDF compared with the next-to-leading-order prediction from JETRAD with CTEQ4M and $\mu = E_T^{\max}/2$ and $R_{\text{sep}} = 1.3$. The error bars indicate the statistical and systematic uncertainties added in quadrature.

Figure 26 shows the percentage difference between the data and theory relative to the theory. Like DØ's inclusive jet measurement, the dijet mass measurement is in good agreement with theory, well within systematic uncertainties. At larger rapidity, the data tend to be slightly above the predictions at high E_T, as in the CDF data. A χ^2 comparison between data and theory similar to those described in Section 4 shows excellent agreement. As Figure 27 illustrates, the measurement is sensitive to the PDF choice, but unfortunately the significance of that sensitivity is obscured by the systematic uncertainties. As is true of the inclusive jet cross section, these uncertainties are highly correlated. Figure 28 compares the DØ result for $|\eta| \leq 1.0$ with the CDF result and with predictions using CTEQ4M. The kinematic cuts of the two analyses overlap significantly; 59% of the CDF sample has the two leading jets with $|\eta| \leq 1.0$. There is remarkable agreement between these data samples over the full mass range.

7.3 The Dijet Angular Distributions

The dijet angular distribution measured in the center of mass is sensitive primarily to the hard scattering matrix elements. In fact, the distribution is unique among

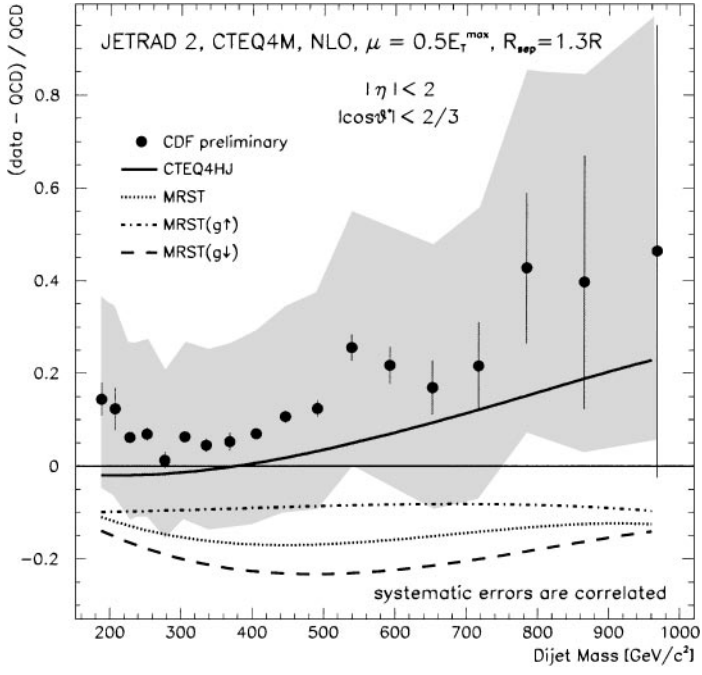

Figure 25 CDF data compared with predictions from the JETRAD program for CTEQ4M and $\mu = E_T^{\max}/2$ and $R_{\text{sep}} = 1.3$ (solid circles). Predictions using other parton distribution functions and $\mu = E_T^{\max}/2$ are also compared with CTEQ4M: MRST (dotted), CTEQ4M with $\mu = E_T^{\max}$ (dashed), and CTEQ4HJ (solid). The error bars indicate the statistical errors. The shaded area represents the combined systematic uncertainty.

high-E_T measurements in that it is almost independent of the PDFs. The shape of the angular distribution is dominated by *t*-channel exchange and is nearly identical for all dominant scattering subprocesses (e.g. $gg \to gg, qg \to qg$, and $qq \to qq$). The dijet angular distribution predicted by LO QCD (two jets only) is roughly proportional to the Rutherford cross section

$$\frac{d\sigma}{d\cos\theta^*} \propto \frac{1}{\sin^4(\theta^*/2)}.$$

To flatten the distribution and facilitate the comparison with theory, the variable transformation $\chi = \frac{1+|\cos\theta^*|}{1-|\cos\theta^*|}$ is used, giving

$$\frac{d^3\sigma}{dM_{jj}\, d\chi\, d\eta_{\text{boost}}}.$$

For measurement of the dijet angular spectra, this quantity is integrated over η_{boost} and mass regions and normalized to the total number of events N in those

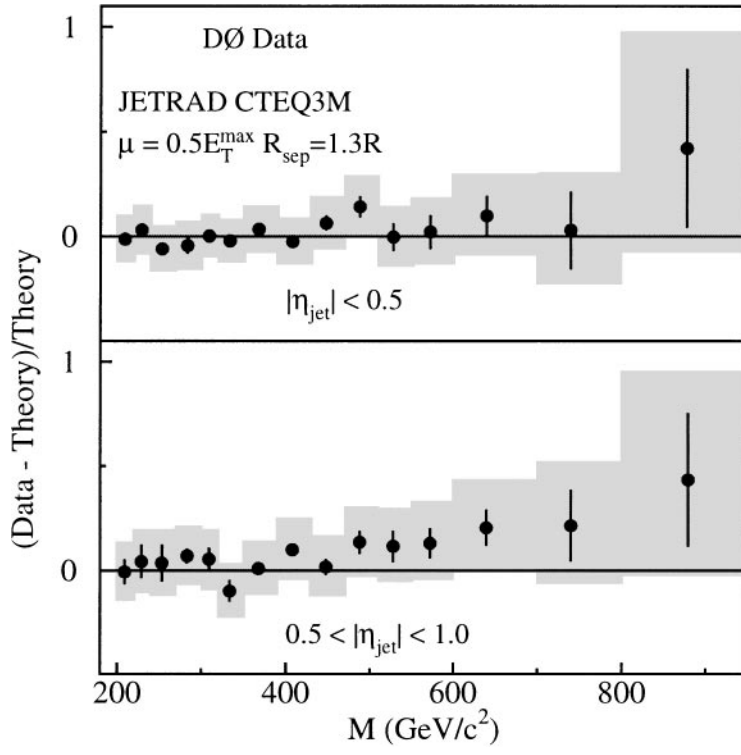

Figure 26 The difference between the DØ dijet mass data and the prediction (JETRAD) divided by the prediction for $|\eta_{\text{jet}}| \leq 0.5$ and $0.5 < |\eta_{\text{jet}}| < 1.0$. The solid circles represent the comparison to the calculation using CTEQ3M with $\mu = 0.5E_T^{\max}$. The shaded region represents the $\pm 1\sigma$ systematic uncertainties.

regions. The normalization reduces both experimental and theoretical uncertainties. Figure 29 shows the $\frac{1}{N}\frac{dN}{d\chi}$ distributions from the DØ collaboration for four mass ranges (53). In all cases, the jets are limited to regions of full acceptance. The NLO predictions from JETRAD with $\mu = E_T^{\max}$ provide the best agreement with the shape of the data. The large χ acceptance of the measurement allows discrimination between LO and NLO predictions. Figure 30 compares CDF data with QCD predictions (JETRAD) for different mass bins (54). In this case, both LO and NLO QCD are in good agreement with the distribution.

7.4 Compositeness and New Physics Limits

The dijet mass and angular distributions are sensitive to new physics such as quark compositeness. In QCD parton-parton scattering, the dominant exchange involves the t-channel. This produces distributions peaked at small center-of-mass scattering

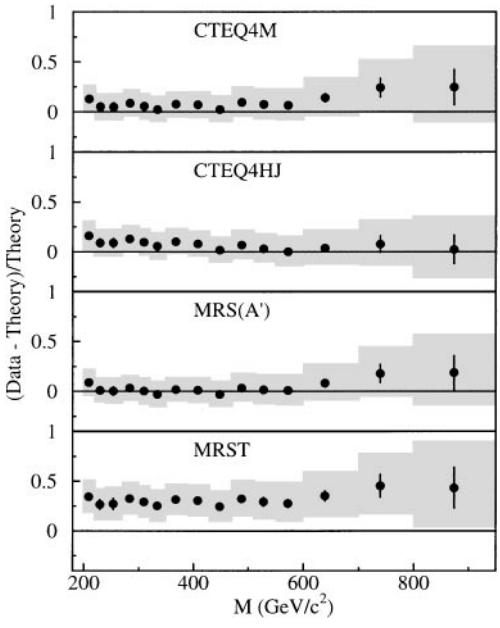

Figure 27 For $|\eta_{\text{jet}}| < 1.0$, the percentage difference between the DØ dijet mass data and JETRAD predictions. The calculations used $\mu = 0.5 p_T^{\max}$, $R_{\text{sep}} = 1.3$ and CTEQ4M, CTEQ4HJ, MRS(A′), and MRST. The error bars represent the statistical uncertainty on the data. The shaded region represents the $\pm 1\sigma$ systematic uncertainties.

angles (near the beam axis in the laboratory), e.g. large η and χ. In contrast, the compositeness model (11) predicts a more isotropic angular distribution. Thus, relative to QCD predictions, the contributions of composite quarks would be most noticeable in the central region, near $\eta = 0$ and $\chi = 1$.

Compositeness signals may be parameterized by a mass scale Λ which characterizes the quark-substructure coupling. Limits on Λ are set assuming that $\Lambda \gg \sqrt{\hat{s}}$ such that the dominant force is still QCD. The substructure coupling is approximated by a four-Fermi contact interaction giving rise to an effective Lagrangian (11). The Lagrangian contains eight terms describing the coupling of left- and right-handed quarks and antiquarks. Currently, only the term describing the left-handed coupling of quarks and antiquarks has been calculated, and this term has an unknown phase. Limits are reported for the case in which specific quarks or all quarks are composite with either constructive interference (Λ^-) or destructive interference (Λ^+). To set compositeness limits, CDF and DØ both use the NLO JETRAD prediction times a k-factor from LO QCD plus compositeness (54). NLO calculations with compositeness are not available. Figure 30 includes a curve with a compositeness signal added. The additional contribution at low χ is most pronounced in the highest dijet mass bins.

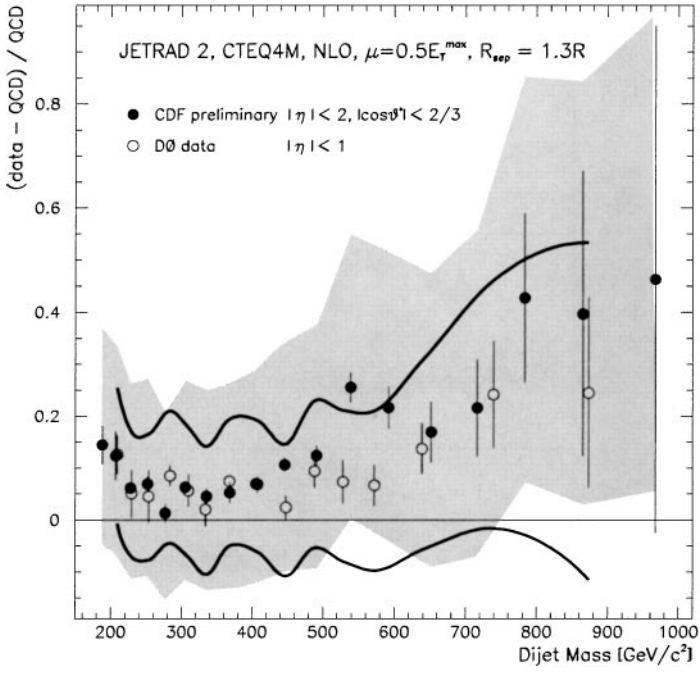

Figure 28 DØ (open circles) and preliminary CDF (solid circles) dijet mass results compared with predictions from the JETRAD program for CTEQ4M and $\mu = E_T/2$. Solid lines, DØ systematic error; shaded area, CDF systematic error.

Both CDF and DØ set compositeness limits based on the ratio of number of events at low χ to those in the high-χ region. Figure 31 shows the CDF result for the ratio of the number of events below $\chi = 2.5$ and between $\chi = 2.5$ and $\chi = 5.0$ as a function of the dijet mass, along with curves that correspond to the different values of Λ. Using this ratio, the CDF data exclude at the 95% confidence level a contact interaction scale of $\Lambda^+_{ud} \leq 1.6$ TeV and $\Lambda^-_{ud} \leq 1.4$ TeV. For a model in which all quarks are composite, the limits are $\Lambda^+ \leq 1.8$ TeV and $\Lambda^- \leq 1.6$ TeV. Figure 32 shows the angular distribution as measured by DØ for very high dijet masses (greater than 635 GeV/c^2) compared with predictions that include composite quarks. Compositeness limits in this analysis are derived from the ratio of the number of events above and below $\chi = 4$. The data exclude (at the 95% confidence level) the following contact interaction scales with $\mu = 1.0E_T^{\max}$: $\Lambda^-_{ud} \leq 2.0$ TeV, $\Lambda^- \leq 2.2$ TeV, $\Lambda^+ \leq 2.1$ TeV. With $\mu = 0.5E_T^{\max}$, the data exclude $\Lambda^-_{ud} \leq 2.2$ TeV, $\Lambda^- \leq 2.4$ TeV, and $\Lambda^+ \leq 2.3$ TeV.

The best limits on compositeness now come from recent dijet mass measurements by the DØ collaboration (52), which combine the sensitivity of the dijet mass distributions with the PDF independence of the angular distributions. In

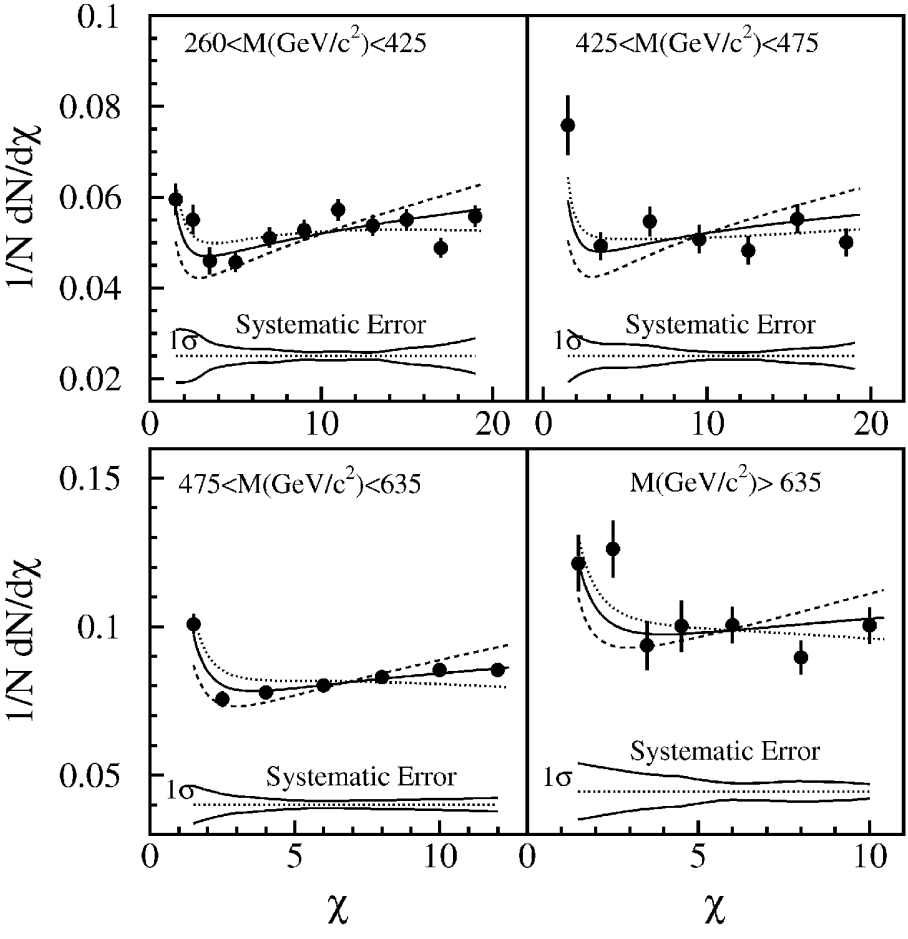

Figure 29 Dijet angular distribution as measured by DØ for different mass ranges compared with leading-order and next-to-leading-order QCD predictions. Dotted line, $\mathrm{NLO}_\mu = 0.5E_T^{\max}$; solid line, $\mathrm{NLO}_\mu = E_T^{\max}$; dashed line, $\mathrm{LO}_\mu = 0.5E_T^{\max}$.

much the same way that jet production from a composite interaction increases the χ spectrum at low values of χ, the dijet mass spectrum increases at central rapidities relative to forward rapidities. Thus, the ratio of the central and forward dijet mass spectra are sensitive to Λ. In addition, both theoretical and experimental uncertainty are reduced in the ratio. Figure 33 shows the ratio of cross sections for $|\eta_{\mathrm{jet}}| \leq 0.5$ and $0.5 \leq |\eta_{\mathrm{jet}}| \leq 1.0$ as a function of dijet mass. As indicated by the family of curves, the compositeness model predicts changes in shape to this ratio at high mass. The spectrum rules out quark compositeness at the 95% confidence level for Λ^+ below 2.7 TeV and Λ^- below 2.5 TeV.

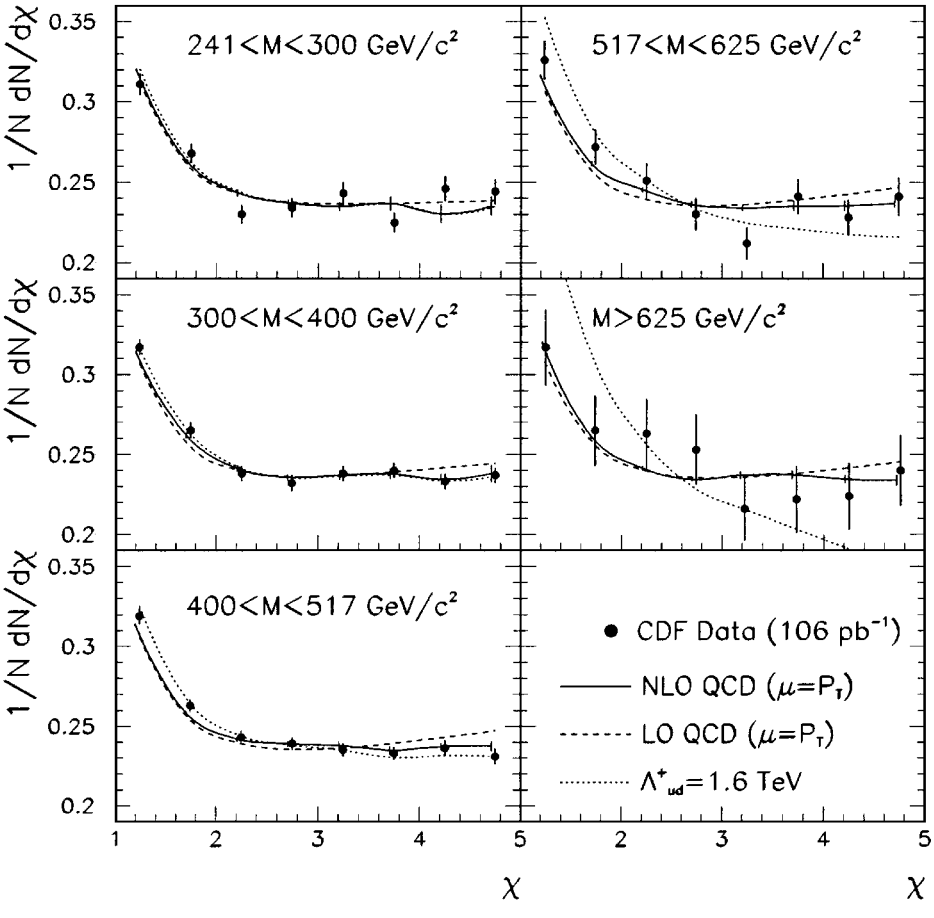

Figure 30 Dijet angular distribution as measured by CDF for different mass ranges compared with leading-order and next-to-leading-order QCD predictions.

8. CONCLUSIONS

The inclusive jet and dijet cross sections provide fundamental tests of QCD predictions at the highest jet E_T and thus are the deepest probes into the structure of the proton. With the increased luminosity delivered by the Tevatron, measurements of these cross sections are no longer limited by statistical uncertainties. In fact, the systematic uncertainties from the experimental measurements and from the theoretical predictions are comparable in size and are significantly larger than the statistical uncertainty on all but the highest E_T data. Uncertainties in the PDFs dominate the theoretical uncertainty, whereas uncertainties in the jet energy scale dominate the experimental measurements.

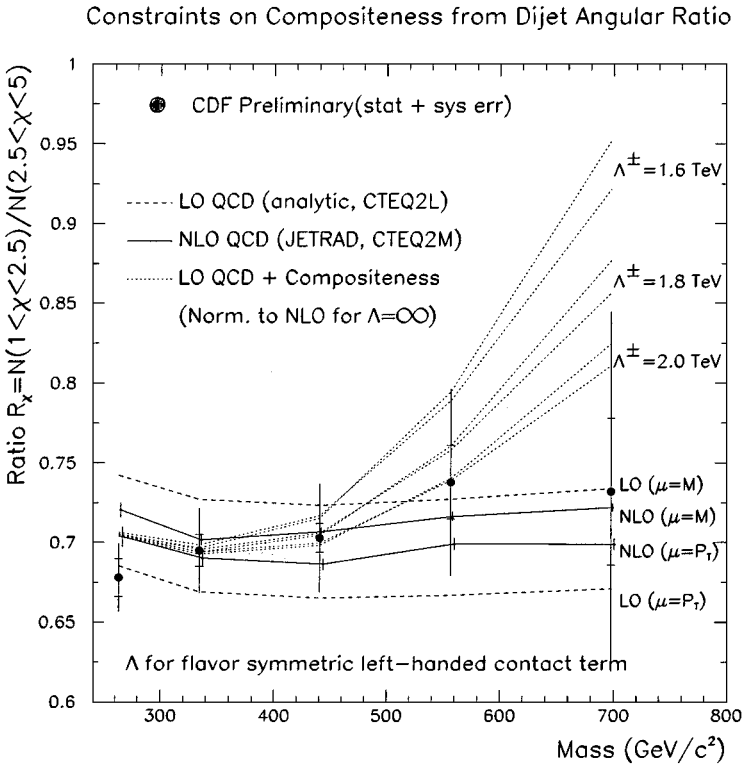

Figure 31 Dijet angular distribution as measured by CDF compared with QCD and with QCD plus a term for composite quarks. Limits on compositeness are derived from the dijet angular distribution ratio of the number events below $\chi = 2.5$ to the number between 2.5 and 5.

The inclusive jet cross sections from the Tevatron have proved a particularly interesting test of QCD. The Run 1A inclusive jet measurement showed disagreement with concurrent pQCD predictions at the highest x and Q. Two subsequent measurements, each using five times the data, show mixed agreement between the data and theory at high E_T. One measurement is consistent with the Run 1A measurement and can be described by QCD if the PDFs are suitably modified. The second Run 1B measurement is well described by QCD with PDFs that either do or do not include high-E_T jet data. Furthermore, within statistical and systematic errors, the three measurements are compatible. The preliminary measurements of the inclusive jet cross section at $\sqrt{s} = 630$ GeV and the ratio of the cross sections show good agreement with previous results and marginal agreement with QCD predictions. Derivation of quantitative results is in progress. Unfortunately, this sample is too statistically limited to provide a constraint on the high-E_T behavior of the cross section at 1800 GeV.

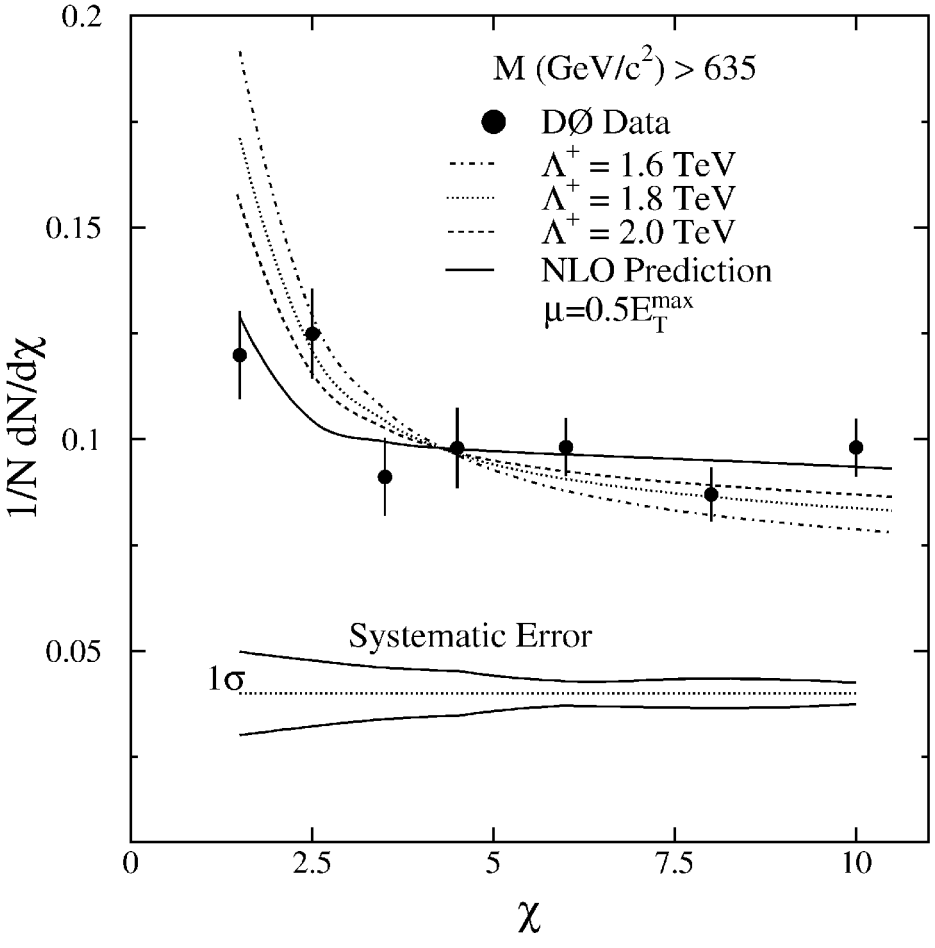

Figure 32 Dijet angular distribution as measured by DØ compared with predictions that include additional contributions from composite quarks.

The apparent excess of events at high E_T observed in the inclusive jet cross section from Run 1A triggered intense scrutiny of the theoretical predictions. This has resulted in a better understanding of the uncertainty in the theoretical predictions, particularly for the PDFs. The dijet mass distributions and differential cross sections reflect a story similar to that of the inclusive jet measurements. The results are generally consistent with each other and with QCD, but data in the moderately forward regions hint that some high-*x* modifications of the PDFs might be appropriate. Incorporation of this information into the global fitting procedures used to derive the PDFs should be particularly helpful in reducing the uncertainty

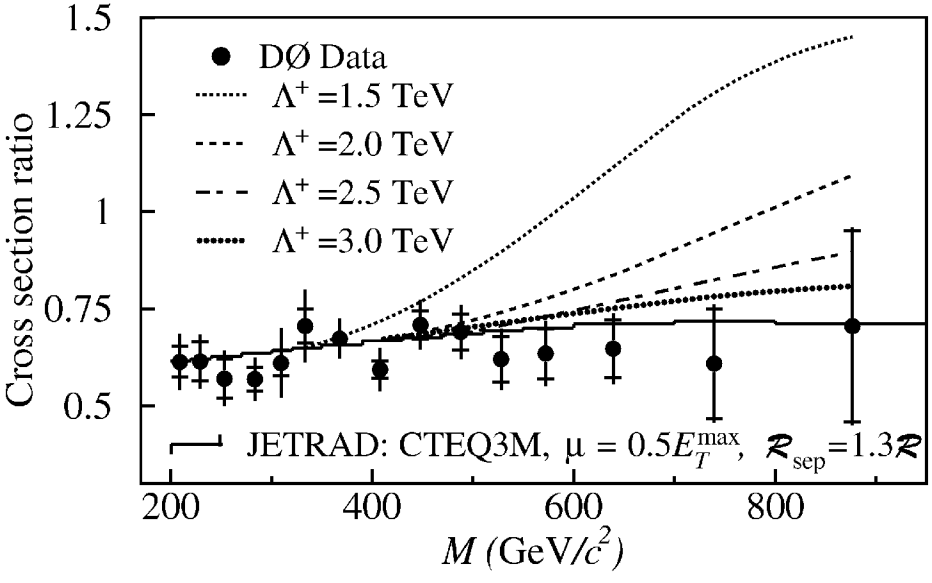

Figure 33 The ratio of DØ dijet mass cross sections for $|\eta_{\rm jet}| < 0.5$ and $0.5 < |\eta_{\rm jet}| < 1.0$ for data (solid circles) and theory (various lines). The error bars show the statistical and systematic uncertainties added in quadrature, and the crossbar shows the size of the statistical error.

associated with extrapolation from low-energy DIS data to the kinematic region covered by the Tevatron jet measurements.

Until the uncertainty in the PDFs is reduced or a method to analytically evaluate their uncertainties becomes available, the best limits on compositeness will come from measurements insensitive to the PDFs, and particularly measurements that rely on angular information. According to these angular distributions, the partonic hard scattering is well described by NLO theoretical calculations. Comparisons of the angular and mass data to jet-production models augmented by quark compositeness show no deviations from standard QCD predictions. In fact, the analyses now indicate that the compositeness scale must be greater than 2.5 TeV if it exists at all.

The high-precision Tevatron jet data have fostered great progress in our understanding of QCD. Thanks to the flexibility of theoretical predictions, pQCD can describe nearly all inclusive jet and dijet observations. Limits on quark substructure from Run 1 have nearly doubled from the previous measurements. However, more stringent tests will require improved PDFs and reduced theoretical uncertainties. Expectations are high that the experimental measurements of jets and their properties will continue to improve during Run 2 with a 20-fold increase in

data sample size, increased beam energy from the upgraded accelerators, and with reduced systematic uncertainties from the upgraded detectors.

ACKNOWLEDGMENTS

We wish to thank the members of the CDF and DØ collaborations for permitting us to include their results. In particular we would like to thank Iain Bertrum, Anwar Bhatti, Frank Chlebana, Bjoern Hinrichsen, Bob Hirosky, and John Krane for helpful discussions during preparation of this review and for providing excellent illustrations.

LITERATURE CITED

1. Akesson T, et al (AFS Collaboration). *Phys. Lett.* B123:133 (1983)
2. Appel J, et al (UA2 Collaboration). *Phys. Lett.* B160:349 (1985); Alitti J, et al (UA2 Collaboration). *Phys. Lett.* B257:232 (1991)
3. Arnison G, et al (UA1 Collaboration). *Phys. Lett.* B172:461 (1986)
4. Abe F, et al (CDF Collaboration). *Phys. Rev. Lett.* 62:613 (1989)
5. Abe F, et al (CDF Collaboration). *Phys. Rev. Lett.* 68:1104 (1992)
6. Albajar C, et al (UA1 Collaboration). *Phys. Lett.* B209:127 (1988)
7. Alitti J, et al (UA2 Collaboration). *Zeit. Phys.* B49:17 (1991)
8. Abe F, et al (CDF Collaboration). *Phys. Rev. Lett.* 71:2542 (1993)
9. Abe F, et al (CDF Collaboration). *Phys. Rev. Lett.* 62:3020 (1989)
10. Abe F, et al (CDF Collaboration). *Phys. Rev. Lett.* 69:2896 (1992)
11. Eichten E, Lane K, Peskin M. *Phys. Rev. Lett.* 50:811 (1983), Fermilab-Conf-96/298-T
12. Huth E, Mangano ML. *Annu. Rev. Nucl. Part. Sci.* 43:585 (1993)
13. Abe F, et al (CDF Collaboration). *Phys. Rev. Lett.* 77:438 (1996).
14. Soper D. Presented at 28th Int. Conf. High Energy Phys., Warsaw, Poland, Jul. 1996. hep-ph/9610434, OITS-619 (1996)
15. Stirling WJ. In *Proc. 17th Int. Conf. Phys. in Collision*, Bristol, England, 1997, p. 243. Singapore: World Sci. (1998)
16. Abbott B, et al. *Eur. Phys. J.* C5:687 (1998)
17. Huston J (CDF Collaboration). In *Proc. 29th Int. Conf. High-Energy Phys. (ICHEP 98)*, Vancouver, Canada, 23–29 Jul 1998. In press (1999)
18. Abbott B, et al (DØ Collaboration). *Phys. Rev. Lett.* In press (1999). hep–ph/9807018
19. Ellis RK, Stirling WJ, Webber BR. *QCD and Collider Physics*. Cambridge, UK: Cambridge Univ. Press (1996)
20. Ellis SD, Kunszt Z, Soper DE. *Phys. Rev. Lett.* 64:2121 (1990)
21. Aversa F, et al. *Phys. Rev. Lett.* 65:401 (1990)
22. Giele WT, Glover EWN, Kosower DA. *Phys. Rev. Lett.* 73:2019 (1994)
23. Ellis SD, Kunszt Z, Soper DE. http://zebu.uoregon.edu/soper EKS Jets/jet.html (1999)
24. Giele W. http://www-theory.fnal.gov/ people/giele/giele. html (1999)
25. Huth J, et al. In *Proc. 1990 Summer Study on High Energy Phys.*, ed. E Berger. Singapore: World Sci. (1992)
26. Ellis SK, Kunszt Z, Soper D. *Phys. Rev. Lett.* 69:3615 (1992); Ellis S. CERN-TH-6861-93, June 1993. Presented at 28th Rencontres de Moriond: QCD and High Energy Hadronic Interactions, Les

Arcs, France, 20–27 March 1993. hep–ph/9306280
27. Abbott B, et al. Fermilab-Pub-97-242-E (1997)
28. Botts J, et al (CTEQ Collaboration). *Phys. Lett.* B304:159 (1993)
29. Lai HL, et al. *Phys. Rev. D* 51:4763 (1995)
30. Martin AD, Roberts RG, Stirling WJ. *Phys. Lett.* B354:154 (1995)
31. Lai HL, et al. *Phys. Rev. D* 55:1280 (1997)
32. Martin AD, et al. *Eur. Phys. J.* C4:463 (1998). hep-ph/9803445
33. Huston J, et al. *Phys. Rev. D* 58:114034 (1998). hep-ph/9801444
34. Yang UK, Bodek A. Presented at 29th Int. Conf. High-Energy Physics (ICHEP 98), Vancouver, Canada, July 23–29, 1998. hep-ph/9809480
35. Abe F, et al (CDF Collaboration). NIM Res., A271:387 (1988) and references therein; Abe F, et al (CDF Collaboration). *Phys. Rev. D* 50:2966 (1994)
36. Abachi S, et al (DØ Collaboration). *Nucl. Instrum. Methods* A338:185 (1994)
37. Albrow M, et al. CDF NOTE 4844, FERMILAB-TM-2071(1999)
38. Abe F, et al (CDF Collaboration). *Phys. Rev. D* 50:5550 (1994)
39. Bantly J, et al. FERMILAB-TM-1930, Mar. (1996)
40. Abbott B, et al. *Nucl. Instr. Methods A* In press (1999). hep-ex/9805009 (1998)
41. Deleted in proof
42. Haber C, et al. *Nucl. Instrum. Methods* A289:388 (1990)
43. Abe F, et al (CDF Collaboration). *Phys. Rev. D* 47:4857 (1993)
44. Abe F, et al (CDF Collaboration). *Phys. Rev. D* 45:1448 (1992)
45. Abe F, et al (CDF Collaboration). *Phys. Rev. Lett.* 70:1376 (1993)
46. Abe F, et al (CDF Collaboration). *Phys. Rev. D* 59:052002 (1999), FERMILAB-PUB-98/280-E
47. Hirosky B, Bedeschi F. Presented at Hadron Collider Phys. Workshop XIII, Jan. 14–20, 1999, Bombay, India
48. Huston J. In *Proc. 29th Int. Conf. on High-Energy Phys. (ICHEP 98)*, Vancouver, Canada, 23–29 July 1998. Singapore: World Sci. (1999) MSUHEP-90119, hep-ph/9901352
49. Blazey G. In *Proc. 29th Int. Conf. High-Energy Phys. (ICHEP 98)*, Vancouver, Canada, 23–29 July 1998. Singapore: World Sci. (1999) FNAL-98-367-E. Krane J. *The ratio of inclusive jet cross sections at* $\sqrt{s} = 630$ *GeV and* $\sqrt{s} = 1800$ GeV. PhD thesis. Univ. Nebraska, Lincoln (1998)
50. DiLoretto G. *The triple differential dijet cross section at* $\sqrt{s} = 1.8$ *TeV*. PhD thesis. Mich. State Univ., East Lansing, Mich. (1998)
51. Ellis RK, Sexton J. *Nucl. Phys.* B269:445 (1986)
52. Abbott B, et al (DØ Collaboration). *Phys. Rev. Lett.* In press (1999)
53. Abbott B, et al (DØ Collaboration). *Phys. Rev. Lett.* 80:666 (1998)
54. Abe F, et al (CDF Collaboration). *Phys. Rev. Lett.* 77:5336 (1996); Erratum, 78:4307 (1997)

Annual Review of Nuclear and Particle Science
Volume 49, 1999

CONTENTS